



# Modeling atmospheric mineral aerosol chemistry to predict heterogeneous photooxidation of SO<sub>2</sub>

Zechen Yu, Myoseon Jang, and Jiyeon Park

Department of Environmental Engineering Sciences, Engineering School of Sustainable Infrastructure and Environment, University of Florida, P.O. Box 116450 Gainesville, FL 32611, USA

Correspondence to: Myoseon Jang (mjang@ufl.edu)

Received: 8 February 2017 – Discussion started: 9 March 2017

Revised: 16 July 2017 – Accepted: 17 July 2017 – Published: 25 August 2017

**Abstract.** The photocatalytic ability of airborne mineral dust particles is known to heterogeneously promote SO<sub>2</sub> oxidation, but prediction of this phenomenon is not fully taken into account by current models. In this study, the Atmospheric Mineral Aerosol Reaction (AMAR) model was developed to capture the influence of air-suspended mineral dust particles on sulfate formation in various environments. In the model, SO<sub>2</sub> oxidation proceeds in three phases including the gas phase, the inorganic-salts aqueous phase (non-dust phase), and the dust phase. Dust chemistry is described as the absorption–desorption kinetics of SO<sub>2</sub> and NO<sub>x</sub> (partitioning between the gas phase and the multilayer coated dust). The reaction of absorbed SO<sub>2</sub> on dust particles occurs via two major paths: autoxidation of SO<sub>2</sub> in open air and photocatalytic mechanisms under UV light. The kinetic mechanism of autoxidation was first leveraged using controlled indoor chamber data in the presence of Arizona Test Dust (ATD) particles without UV light, and then extended to photochemistry. With UV light, SO<sub>2</sub> photooxidation was promoted by surface oxidants (OH radicals) that are generated via the photocatalysis of semiconducting metal oxides (electron–hole theory) of ATD particles. This photocatalytic rate constant was derived from the integration of the combinational product of the dust absorbance spectrum and wave-dependent actinic flux for the full range of wavelengths of the light source. The predicted concentrations of sulfate and nitrate using the AMAR model agreed well with outdoor chamber data that were produced under natural sunlight. For seven consecutive hours of photooxidation of SO<sub>2</sub> in an outdoor chamber, dust chemistry at the low NO<sub>x</sub> level was attributed to 55 % of total sulfate (56 ppb SO<sub>2</sub>, 290 µg m<sup>-3</sup> ATD, and NO<sub>x</sub> less than 5 ppb). At high NO<sub>x</sub> (> 50 ppb of NO<sub>x</sub> with low hydrocar-

bons), sulfate formation was also greatly promoted by dust chemistry, but it was suppressed by the competition between NO<sub>2</sub> and SO<sub>2</sub>, which both consume the dust-surface oxidants (OH radicals or ozone).

## 1 Introduction

The surface of mineral dust particles is able to act as a sink for various atmospheric trace gases such as sulfur dioxide (SO<sub>2</sub>), nitrogen oxides (NO<sub>x</sub>, e.g., NO and NO<sub>2</sub>), and ozone (O<sub>3</sub>). Among trace gases, SO<sub>2</sub> has received much attention because heterogeneous oxidation of SO<sub>2</sub> produces non-volatile sulfuric acid, which is readily involved in the acidification of particles or the reaction with dust constituents such as alkaline metals (K<sup>+</sup>, Na<sup>+</sup>) or metal oxides (e.g.,  $\alpha$ -Al<sub>2</sub>O<sub>3</sub> and Fe<sub>2</sub>O<sub>3</sub>). Such modification of the chemical composition of dust particles can influence the hygroscopic properties of mineral dust, which is essential to activate cloud condensation nucleation (Krueger et al., 2003; Zhang and Chan, 2002; Vlasenko et al., 2006; Liu et al., 2008; Tang et al., 2016).

Metal oxides (e.g., TiO<sub>2</sub> and Al<sub>2</sub>O<sub>3</sub>) have frequently been used in many laboratories to study the key role of mineral dust in the heterogeneous oxidation of SO<sub>2</sub> (Goodman et al., 2001; Usher et al., 2002; Zhang et al., 2006). However, these laboratory studies have been limited to a certain type of metal oxide and autoxidation of SO<sub>2</sub> without a light source. To date, only a few studies have attempted to study the photocatalytic characteristics of mineral dust in the oxidation of SO<sub>2</sub> and NO<sub>x</sub>. For example, as noted by Park and Jang (2016), the reactive uptake coefficient ( $\gamma_{SO_4^{2-}}$ ) of SO<sub>2</sub> in the presence of dry Arizona Test Dust (ATD) particles under UV light was

1 order of magnitude higher ( $1.16 \times 10^{-6}$  using an indoor chamber with a light mix of UV-A and UV-B light) than that from autoxidation ( $1.15 \times 10^{-7}$ ) without a light source. Using an aerosol flow tube, Dupart et al. (2014) observed that the uptake rate of  $\text{NO}_2$  by ATD dust particles was significantly enhanced (by 4 times) under UV-A irradiation compared to dark conditions. Field observations have also reported the promotion of  $\text{SO}_2$  photooxidation in the presence of mineral dust. For instance, near Beijing, China (ground-based campaign in 2009), and in Lyon, France (remote-sensing campaign in 2010), Dupart et al. (2012) found that mineral dust was a source of OH radicals under UV radiation that promoted sulfate formation.

Semiconducting metal oxides (e.g.,  $\alpha\text{-Al}_2\text{O}_3$ ,  $\alpha\text{-Fe}_2\text{O}_3$ , and  $\text{TiO}_2$ ) act as a photocatalyst in mineral dust particles that can yield electron ( $e_{\text{cb}}^-$ )-hole ( $h_{\text{vb}}^+$ ) pairs, and that they are involved in the production of strong oxidizers, such as superoxide radical anions ( $\text{O}_2^-$ ) and OH radicals (Linsebigler et al., 1995; Hoffmann et al., 1995; Thompson and Yates, 2006; Cwiertny et al., 2008; Chen et al., 2012; Dupart et al., 2014; Colmenares and Luque, 2014). These oxidizers enable rapid oxidation of adsorbed  $\text{SO}_2$  and  $\text{NO}_x$  on the surface of mineral dust particles. For example, using transmission Fourier transform infrared (FTIR) spectroscopy and X-ray photoelectron spectroscopy, Nanayakkara et al. (2012) observed the oxidation of  $\text{SO}_2$  by the photocatalytically generated OH radicals in the presence of titanium oxide particles. The heterogeneous formation of sulfate and nitrate can be highly variable and dependent on the chemical characteristics of dust aerosol (Gankanda et al., 2016). Authentic mineral dust particles differ from pure metal oxides in chemical composition. For example, Wagner et al. (2012) reported that the content of metal oxides in Saharan dust samples collected from Burkina Faso includes 14 %  $\text{Al}_2\text{O}_3$ , 8.4 %  $\text{Fe}_2\text{O}_3$ , and 1.2 %  $\text{TiO}_2$ .

Most research on dust photochemistry has been limited to qualitative studies and lacks kinetic mechanisms that are linked to a predictive model. The typical wave-dependent photolysis of gas-phase trace gases has long been subject to atmospheric photochemistry. This photolysis rate is a first-order reaction and is calculated via the coupling actinic flux (the quantity of photons) with the characteristics (cross section area and quantum yield) of a light-absorbing molecule (McNaught and Wilkinson, 1997). In order to model dust photochemistry, the integration of wavelength-dependent actinic flux with the photocatalytic activity of mineral dust is needed.

In addition to sunlight intensity, humidity also influences heterogeneous dust chemistry. Humidity governs particle water content, which influences the gas–dust sorption process of trace gases (Navea et al., 2010) and the formation of dust-phase oxidants. Huang et al. (2015) found that the  $\gamma_{\text{SO}_4^{2-}}$  of  $\text{SO}_2$  autoxidation in ATD particles increased by 142 % because the relative humidity (RH) changed from 15 to 90 %. In the presence of UV light, the particle water content can

act as an acceptor for  $h_{\text{vb}}^+$  and produce surface OH radicals, promoting heterogeneous photochemistry of  $\text{SO}_2$  on mineral dust. In the presence of UV light, Shang et al. (2010) reported that sulfate production on the surface of  $\text{TiO}_2$  increased by 5 times because of the increase in RH from 20 to 80 %. Park and Jang (2016) also reported the exponential increase in  $\gamma_{\text{SO}_4^{2-}}$  as the RH increased from 20 to 80 % for both autoxidation and photooxidation of  $\text{SO}_2$  in the presence of ATD particles. A few studies have attempted to simulate sulfate formation in the presence of mineral dust at regional scales using laboratory-generated kinetic parameters (Tang et al., 2004; Li and Han, 2010; Dong et al., 2016). However,  $\gamma_{\text{SO}_4^{2-}}$  applied to the regional simulations originated from pure and dry metal oxides without UV light, and thus will differ from those of ambient dust exposed to natural sunlight. It is expected that the typical regional simulations during dust events might underestimate the formation of sulfate.

In this study, the Atmospheric Mineral Aerosol Reaction (AMAR) model was developed to predict atmospheric oxidation of trace gases such as  $\text{SO}_2$  and  $\text{NO}_2$  under ambient conditions. The kinetic mechanisms of dust-driven photochemistry, including autoxidation and photooxidation of  $\text{SO}_2$ , were newly established in the model. The rate constant of dust photoactivation, which forms electron–hole pairs and sources dust-driven oxidants, was integrated into the model. The influence of meteorological variables, such as humidity, temperature, and sunlight, on  $\text{SO}_2$  oxidation was investigated using the resulting AMAR model. The model also addresses the kinetic mechanism to simulate how atmospheric major pollutants such as  $\text{NO}_x$  and ozone are engaged in the oxidation of  $\text{SO}_2$  in the presence of airborne dust particles. For environmental scenarios, the model was applied for polluted urban conditions (e.g., hydrocarbon ppbC /  $\text{NO}_x$  ppb < 5) and low- $\text{NO}_x$  conditions (e.g., hydrocarbon ppbC /  $\text{NO}_x$  ppb < 5). The reaction rate constants for both autoxidation and photocatalytic reactions of  $\text{SO}_2$  were obtained through the simulation of indoor chamber data, which were previously generated under various meteorological and environmental conditions (Park and Jang, 2016). The suitability of the resulting AMAR model was tested against sulfate formation in a large outdoor smog chamber at the University of Florida Atmospheric Photochemical Outdoor Reactor (UF-APHOR) under natural sunlight. The AMAR model of this study will vastly improve the accuracy of the prediction of sulfate and nitrate formation in regional and global scales where dust emission is influential.

## 2 Experimental

### 2.1 Chamber experiments

The indoor chamber data of this study were obtained from the recent laboratory study by Park and Jang (2016) to determine the kinetic rate constants that are needed to develop

the AMAR model. The indoor chamber operation has been reported previously (Park and Jang, 2016) (also see Sect. S1 in the Supplement). The indoor chamber data are listed in Table 1. The outdoor chamber experiments were performed in the UF-APHOR dual-chambers ( $52\text{ m}^3$  for each chamber) to test the suitability of AMAR model to ambient condition. The light irradiation of the indoor-UV light and the sunlight is shown in Fig. S1. A detailed description of the operation of the outdoor chamber is also described in Sect. S1. The outdoor experimental conditions for  $\text{SO}_2$  heterogeneous reaction in the presence of mineral dust particles are listed in Table 2.

## 2.2 Light absorption of ATD particles

The absorbance spectrum of ATD particles was measured to develop the reaction rate constants in the kinetic model. The detailed procedure for light absorption measurement of particle samples can be found in the previous study (Zhong and Jang, 2011). The particle size distribution of ATD is shown in Fig. S2. The suspended dust particles were sampled on a Teflon-coated glass fiber filter for 20 min. The masses difference of dust sample was measured using a microbalance (MX5, Mettler Toledo, Columbus, OH). The light absorbance of the dust filter sample ( $\text{Abs}_{\text{ATD}}$ ) was measured using a Perkin-Elmer Lambda 35 UV-visible spectrophotometer equipped with a Labsphere RSA-PE-20 diffuse-reflectance accessory. The absorbance spectrum was normalized by particle mass and calculated to obtain the mass absorbance cross section (See Sect. S1). The resulting absorbance cross section and quantum yield of ATD dust are shown in Fig. S3.

## 3 AMAR model description

The overall schematic of the AMAR model is shown in Fig. 1. In the model, the total sulfate mass concentration ( $[\text{SO}_4^{2-}]_{\text{T}}$ ,  $\mu\text{g m}^{-3}$ ) is predicted from the reactions in three phases: the sulfate formed in the gas phase ( $[\text{SO}_4^{2-}]_{\text{gas}}$ ,  $\mu\text{g m}^{-3}$ ), the sulfate from the aqueous phase ( $[\text{SO}_4^{2-}]_{\text{aq}}$ ,  $\mu\text{g m}^{-3}$ ), and the sulfate from dust-driven chemistry ( $[\text{SO}_4^{2-}]_{\text{dust}}$ ,  $\mu\text{g m}^{-3}$ ). The key components of the model consist of the partitioning process and the kinetic mechanisms in three phases.

1. The gaseous inorganic species (e.g.,  $\text{SO}_2$ ,  $\text{NO}_x$  and ozone) are partitioned onto both inorganic-salt (sulfuric acid and its salts) seeded aqueous particles and mineral dust particles. ATD particles are known to be coated with the multilayer of water due to their high affinity to water (Gustafsson et al., 2005) (Sect. 3.2.1). Therefore, we assume that gas–dust partitioning of tracers on multilayer water is processed in absorption mode.

2.  $\text{SO}_2$  oxidation in the gas phase is simulated using mechanisms previously reported in the literature (Byun and Schere, 2006; Sarwar et al., 2013, 2014; Binkowski and Roselle, 2003) (Table S1 in the Supplement).
3. The partitioned  $\text{SO}_2$  is heterogeneously oxidized in the inorganic-salt seeded aqueous phase based on the previously reported mechanisms (Liang and Jacobson, 1999).
4. The formation of sulfate ( $[\text{SO}_4^{2-}]_{\text{dust}}$ ) in the dust phase is approached using two kinetic sub-modules: the production of sulfate ( $[\text{SO}_4^{2-}]_{\text{auto}}$ ,  $\mu\text{g m}^{-3}$ ) by autoxidation in open air and sulfate formation ( $[\text{SO}_4^{2-}]_{\text{photo}}$ ,  $\mu\text{g m}^{-3}$ ) by photocatalytic reactions. Overall, dust chemistry within the multilayer of water is treated in a similar manner to aqueous chemistry. However, aqueous chemistry is operated through the whole aerosol volume and dust chemistry is processed in the water layers on the surface of dust particles.

The simulation of chamber data using the model was performed using a kinetic solver (Morpho) (Jeffries, 1998). In these mechanisms, the symbols “g”, “aq”, and “d” denote the chemical species in the gas phase, inorganic-salt seeded aqueous phase, and dust phase, respectively. The unit of the concentration of chemical species is molecule per cubic centimeter of air. The rate constants associated with various reaction mechanisms in the AMAR model were determined by simulating pre-existing indoor chamber data obtained from controlled experimental conditions (Park and Jang, 2016). For example, the rate constant for  $\text{SO}_2$  autoxidation ( $k_{\text{auto}}$ ,  $\text{s}^{-1}$ ) is semiempirically determined by fitting the predicted concentration of sulfate to the experimental data D1 in Table 1. The gas–dust partitioning constant ( $K_{\text{d},\text{SO}_2}$ , Sect. 3.2.1) of  $\text{SO}_2$  is dependent on temperature, aerosol water content, and acidity.  $K_{\text{d},\text{SO}_2}$  values were semiempirically determined using data D1–D3 (three different RHs) and the literature parameters related to the effect of temperature and acidity on  $K_{\text{d},\text{SO}_2}$ . The rate constant ( $k_{\text{photo}}$ ,  $\text{cm}^3 \text{molecule}^{-1} \text{s}^{-1}$ ) for the sulfate formation by photocatalytic reactions is semiempirically determined using data L1–L3 (three different RHs) in Table 1. In the presence of ozone,  $k_{\text{auto}}$  and  $k_{\text{photo}}$  are determined using datasets D4 and L4, respectively. In the following sections, the components of the AMAR model are described in detail.

### 3.1 $\text{SO}_2$ oxidation in gas phase and aerosol aqueous phase

#### 3.1.1 Gas-phase oxidation

The oxidation of  $\text{SO}_2$  in the gas phase has been extensively studied by numerous researchers (Baulch et al., 1984; Kerr, 1984; Atkinson and Lioyd, 1984; Calvert and Stockwell, 1984; Graedel, 1977; Atkinson et al., 1997). In this study,

**Table 1.** Experiment conditions and simulation results for  $\text{SO}_2$  heterogeneous photooxidation on the surface of ATD particles at a variety of humidity conditions (RH), light sources, and initial concentrations of traces using indoor chamber data.

Exp. no. <sup>a</sup>	UV	RH <sup>b</sup> (%)	Temp. <sup>b</sup> (K)	Initial concentration				Duration <sup>e</sup> (min)	Exp. [ $\text{SO}_4^{2-}$ ] <sub>T</sub> ( $\mu\text{g m}^{-3}$ )	Note <sup>g</sup>
				ATD dust <sup>c</sup> ( $\mu\text{g m}^{-3}$ )	$\text{SO}_2^d$ (ppb)	NO / $\text{NO}_2^d$ (ppb)	$\text{O}_3^d$ (ppb)			
D1	Off	21.0	295.9	295	267	n/a	n/a	150	0.61 $\pm$ 0.02	$K_{\text{d},\text{SO}_2}$ , $k_{\text{auto}}$
D2	Off	55.3	295.0	406	152	0.1/0.6	1.86	148	1.02 $\pm$ 0.01	
D3	Off	80.1	294.5	278	147	0.9/1.6	0.29	147	1.59 $\pm$ 0.02	
L1	On	20.4	297.0	123	87.8	0.3/1.7	0.30	120	1.66 $\pm$ 0.04	$k_{\text{OH},\text{O}_2}$ , $k_{\text{auto}}$
L2	On	55.2	299.3	120	82.3	0.2/1.9	1.79	120	2.54 $\pm$ 0.21	
L3	On	80.7	298.7	131	78.0	0.2/0.4	0.28	120	5.22 $\pm$ 0.19	
L4	On	21.0	296.9	130	78.1	0.1/1.35	64.8	120	4.48 $\pm$ 0.14	$k_{\text{OH},\text{O}_3}$
D4	Off	20.4	296.6	293	101.0	0.7/1.9	65.4	60	0.158 $\pm$ 0.01	$k_{\text{auto},\text{O}_3}$

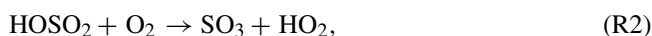
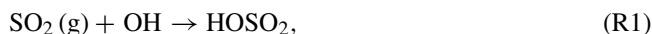
<sup>a</sup> “D” denotes experiments under dark conditions. “L” denotes experiments with UV light. The dataset D1–D3 and L1–L4 were obtained from the recent laboratory data reported by Park and Jang (2016). Dataset D4 was newly added here to estimate the kinetic parameter of heterogeneous autoxidation of  $\text{SO}_2$  in the presence of ozone. <sup>b</sup> The accuracy of RH is  $\pm 5\%$ . The accuracy of temperature is  $\pm 0.5\text{ K}$ . <sup>c</sup> The mass concentration of ATD particles were calculated combining SMPS data, OPC data, the density of dust particles ( $2.65\text{ g cm}^{-3}$ ), and the particle size distribution ( $< 3\text{ }\mu\text{m}$ ). The errors associated with the dust particle mass concentration were  $\pm 6\%$ . <sup>d</sup> The errors associated with the observation of  $\text{SO}_2$ , NO,  $\text{NO}_2$ , and  $\text{O}_3$  were  $\pm 0.9$ ,  $\pm 12.5$ ,  $\pm 6.9$ , and  $\pm 0.2\%$ , respectively. <sup>e</sup> The duration is the simulation time from the beginning of the experiment to the end of the experiment. <sup>f</sup> Sulfate concentrations were measured at the end of experiments using PILS-IC. The measurements were not corrected for the particle loss rate to the wall but corrected for the indigenous sulfate from dust particles. <sup>g</sup> The experiments are noted with the associated kinetic parameters that were empirically determined. n/a = not applicable

**Table 2.** Outdoor chamber experiment condition for  $\text{SO}_2$  heterogeneously photooxidation on the ATD particles at variety initial concentration of  $\text{SO}_2$ , dust particle, and  $\text{NO}_x$ .

Exp. date	Purpose	RH <sup>a</sup> (%)	Temp. <sup>a</sup> (K)	Simulation time (EST)	Initial concentration <sup>b</sup>			
					ATD dust <sup>c</sup> ( $\mu\text{g m}^{-3}$ )	$\text{SO}_2$ (ppb)	NO / $\text{NO}_2$ (ppb)	$\text{O}_3$ (ppb)
28 Mar 2015	$\text{SO}_2$	18–67	277.1–301.9	11:10–16:30	n/a	60.1	0.1/0.9	6.3
28 Mar 2015	$\text{SO}_2$ & dust	15–45	277.8–301.5	10:50–16:30	290.1	56.4	0.1/0.7	0.7
16 Jun 2015	Low dust	15–49	286.7–313.0	08:40–15:30	90.1	100.0	0.1/0.7	0.7
16 Jun 201	High dust	16–48	287.0–311.5	09:30–15:30	403.7	120.1	1.1/1.0	5
12 Nov 2015	Low $\text{SO}_2$	24–71	287.8–312.9	08:40–17:30	239.2	119.0	0.5/2.0	3.0
12 Nov 2015	High $\text{SO}_2$	14–42	287.3–311.06	09:00–17:30	229.0	271.6	0.2/2.1	2.6
14 Apr 2017	$\text{NO}_x$ effect	33–95	287.8–314.3	06:30–17:30	496.2	88.1	88.9/13.5	3.0
25 Apr 2017–1	$\text{NO}_x$ effect	18–89	283.8–313.6	06:00–16:00	414.0	15.0	112.0/13.2	2.2
25 Apr 2017–2	$\text{NO}_x$ effect	26–94	284.1–312.7	06:00–16:00	478.7	17.5	35.9/3.6	1.9

<sup>a</sup> The accuracy of RH is  $\pm 5\%$ . The accuracy of temperature is  $\pm 0.5\text{ K}$ . <sup>b</sup> The errors associated with the observation of  $\text{SO}_2$ , NO,  $\text{NO}_2$ ,  $\text{O}_3$ ,  $\text{NH}_4^+$ , and the concentration of dust particle mass were  $\pm 0.9$ ,  $\pm 12.5$ ,  $\pm 6.9$ ,  $\pm 0.2$ ,  $\pm 5.0$ , and  $\pm 6\%$ , respectively. The detailed observations of the chemical species during the experiments were shown in Figs. S4 and S5 in the Supplement. <sup>c</sup> The mass concentrations of ATD particles were calculated combining SMPS data, OPC data, the density of dust particles ( $2.65\text{ g cm}^{-3}$ ), and the particle size distribution ( $< 3\text{ }\mu\text{m}$ ). n/a = not applicable

the oxidation of  $\text{SO}_2$  is described using comprehensive reaction mechanisms shown in Table S1. The mechanisms can also be simplified as follows:



### 3.1.2 Gas-aerosol partitioning

$\text{SO}_2$  is dissolved into hygroscopic sulfuric acid ( $\text{H}_2\text{SO}_4$ ), which is formed in the gas phase, via a partitioning process and reacts with the aqueous-phase oxidants (e.g.,  $\text{H}_2\text{O}_2$

and  $\text{O}_3$ ) to heterogeneously form  $\text{H}_2\text{SO}_4$ . The chemical species that were treated by the partitioning process include  $\text{SO}_2$ ,  $\text{NO}_x$ ,  $\text{O}_3$ , OH,  $\text{HO}_2$ ,  $\text{H}_2\text{O}_2$ ,  $\text{HCOOH}$ ,  $\text{CH}_3\text{OOH}$ ,  $\text{HNO}_3$ ,  $\text{CH}_3\text{O}_2$ ,  $\text{HONO}$ ,  $\text{CH}_3\text{COOH}$ , and  $\text{HCHO}$ . In the model, the partitioning process is approached using the gas-particle partitioning coefficient  $K_{\text{aq},\text{SO}_2}$  ( $\text{m}^3\text{ }\mu\text{g}^{-1}$ ) based on aerosol mass concentration.  $K_{\text{aq},\text{SO}_2}$  is derived from Henry's law constant of  $\text{SO}_2$  ( $K_{\text{H},\text{SO}_2} = 1.2\text{ mol L}^{-1}\text{ atm}^{-1}$  at 298 K) (Chameides, 1984),

$$K_{\text{aq},\text{SO}_2} = \frac{K_{\text{H},\text{SO}_2}RT}{\rho_{\text{aq}}} \quad (1)$$

where  $R$  is the ideal gas constant ( $\text{J K}^{-1}\text{ mol}^{-1}$ ) and  $\rho_{\text{aq}}$  ( $\text{g cm}^{-3}$ ) is the density of the particle, which is calculated us-

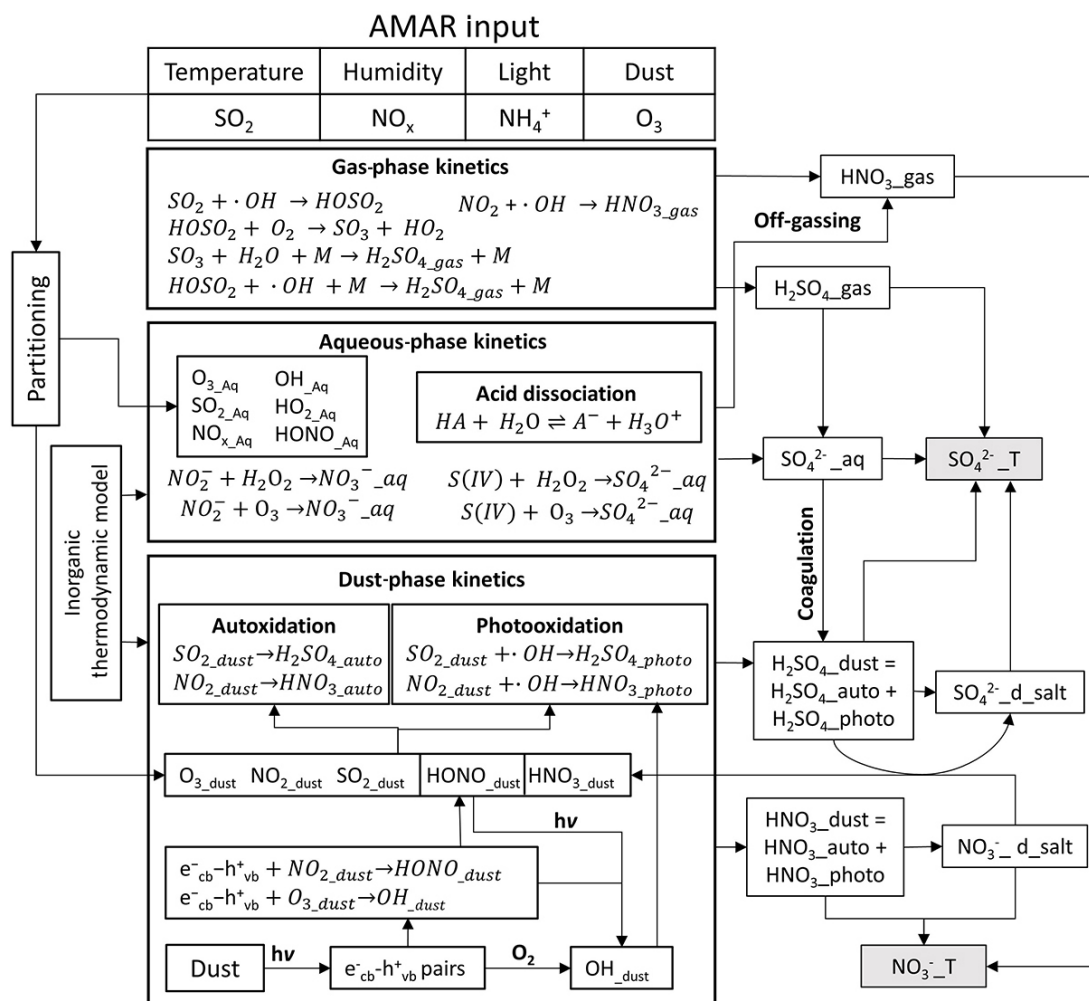
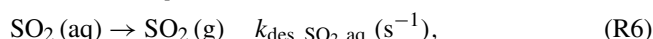
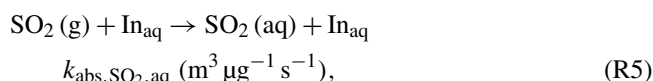


**Figure 1.** The overall schematic of the AMAR model to simulate heterogeneous  $\text{SO}_2$  oxidation. For the description of chemical species, gas phase, aqueous phase, and dust phase are symbolized as “gas”, “aq”, and “dust”, respectively.  $\text{SO}_4^{2-}\text{-T}$ ,  $\text{H}_2\text{SO}_4\text{-gas}$ ,  $\text{SO}_4^{2-}\text{-aq}$ , and  $\text{H}_2\text{SO}_4\text{-dust}$  are the total sulfate formation and the formation of sulfate from gas phase, aqueous phase, and dust phase, respectively.  $\text{SO}_4^{2-}\text{-d\_salt}$  and  $\text{NO}_3\text{-d\_salt}$  are the neutralized sulfate and nitrate in the dust phase.

ing an inorganic thermodynamic model (E-AIM II) (Clegg et al., 1998; Wexler and Clegg, 2002; Clegg and Wexler, 2011) based on humidity and inorganic composition. The partitioning process of  $\text{SO}_2$  on inorganic aerosol ( $\text{In}_{\text{aq}}$ ,  $\mu\text{g m}^{-3}$ ) is expressed as



where  $k_{\text{abs}, \text{SO}_2, \text{aq}}$  ( $\text{m}^3 \mu\text{g}^{-1} \text{s}^{-1}$ ) and  $k_{\text{des}, \text{SO}_2, \text{aq}}$  ( $\text{s}^{-1}$ ) are the uptake rate constant and the desorption rate constant, respectively, and are calculated as follows:

$$k_{\text{abs}, \text{SO}_2, \text{aq}} = f_{\text{abs}, \text{aq}} \frac{\omega_{\text{SO}_2} f_{\text{aq}, \text{S\_M}}}{4}, \quad (2)$$

$$k_{\text{des}, \text{SO}_2, \text{aq}} = \frac{k_{\text{abs}, \text{SO}_2, \text{aq}}}{K_{\text{aq}}}, \quad (3)$$

where  $f_{\text{aq}, \text{S\_M}}$  ( $5 \times 10^{-4}$ ,  $\text{m}^2 \mu\text{g}^{-1}$ ) is the coefficient to convert the aerosol mass concentration ( $\mu\text{g m}^{-3}$ ) to the surface area concentration ( $\text{m}^2 \text{m}^{-3}$ ) for particle size near 100 nm.  $f_{\text{abs}, \text{aq}}$  is the coefficient for uptake process and  $\omega_{\text{SO}_2}$  is the mean molecular velocity ( $\text{m s}^{-1}$ ) of  $\text{SO}_2$  and can be calculated as follows:

$$\omega_{\text{SO}_2} = \sqrt{\frac{8RT}{\pi \text{MW}}}, \quad (4)$$

where MW is molecular weight ( $\text{kg mol}^{-1}$ ). In our model,  $f_{\text{abs}, \text{aq}}$  was set at  $2 \times 10^4$  in Eq. (2) to have fast partition-

ing process. Table S2 summarizes the characteristic time that is estimated for diffusion, partitioning, and the reactions of major species with OH radicals in gas, aqueous, and dust phases. In general, the characteristic time (s) of a partitioning process (order of  $10^{-7}$  s) is much faster than gas-phase oxidation (order of  $10^6$  s), aqueous-phase oxidation (order of  $10^3$ – $10^4$  s), and dust-phase oxidation (order of  $10^2$ – $10^3$  s at presence of  $200 \mu\text{g m}^{-3}$  of dust particles). The mass concentration ( $\mu\text{g m}^{-3}$ ) of inorganic seeded aqueous phase above the efflorescent relative humidity (ERH) is also dynamically calculated for the  $\text{SO}_4^{2-}$ – $\text{NH}_4^+$ – $\text{H}_2\text{O}$  system. Colberg et al. (2003) semiempirically predicted ERH by fitting to the experimental data based on the ammonia-to-sulfate ratio in the  $\text{SO}_4^{2-}$ – $\text{NH}_4^+$ – $\text{H}_2\text{O}$  system. AMAR model utilizes these parameterizations to predict ERH dynamically. Ammonia is inevitable in our chamber study and mainly acts as a carry-over from previous chamber experiments. Thus,  $\text{H}_2\text{SO}_4$  is fully or partially neutralized by ammonia.

### 3.1.3 Aerosol aqueous-phase reaction

The AMAR model implements aqueous-phase chemistry that occurs in inorganic salted aqueous aerosol ( $\text{SO}_4^{2-}$ – $\text{NH}_4^+$ – $\text{H}_2\text{O}$  system without dust) to form  $\text{SO}_4^{2-}$  (aq) and  $\text{NO}_3^-$  (aq). We employed the preexisting aqueous-phase kinetic reactions involving  $\text{SO}_2$  (Liang and Jacobson, 1999) and  $\text{NO}_x$  chemistry (Liang and Jacobson, 1999; Hoyle et al., 2016). Thus, our simulation inherits all the possible uncertainties embedded in the original kinetic data.

The  $\text{SO}_2$  dissolved in the aqueous phase is hydrolyzed into  $\text{H}_2\text{SO}_3$  and dissociates to form ionic species ( $\text{HSO}_3^-$  and  $\text{SO}_3^{2-}$ ).  $\text{SO}_4^{2-}$  (aq) is formed by reactions of the sulfur species in oxidation state IV ((S(IV)) (aq)) with  $\text{OH}$ (aq),  $\text{H}_2\text{O}_2$ (aq), or  $\text{O}_3$ (aq) (Table S1). The dissolved  $\text{HONO}$  can also dissociate to form  $\text{NO}_2^-$  (aq) and result to  $\text{NO}_3^-$  (aq). Each chemical species in S(IV) (aq) has a different reactivity for oxidation reactions. The distribution of chemical species is affected by aerosol acidity, which is controlled by humidity and inorganic composition. Hence, the formation of sulfate is very sensitive to aerosol acidity. For example, most of the S(IV) is consumed by  $\text{H}_2\text{O}_2$  at  $\text{pH} < 4$ , whereas most of it is consumed by  $\text{O}_3$  at  $\text{pH} > 4$ . Some strong inorganic acids, such as sulfuric acid, influence aerosol acidity. In AMAR, aerosol acidity ( $[\text{H}^+]$ ) is estimated at each time step by E-AIM II (Clegg et al., 1998; Wexler and Clegg, 2002; Clegg and Wexler, 2011) corrected for the ammonia-rich condition (Li et al., 2015; Beardsley and Jang, 2016; Li and Jang, 2012) as a function of inorganic composition measured by a particle-into-liquid sampler coupled with ion chromatography (PILS-IC). When the ammonia-to-sulfate ratio is greater than 0.8, the prediction of  $[\text{H}^+]$  is corrected based on the method described by Li and Jang (2012). At high  $\text{NO}_x$  levels,  $\text{NO}_2^-$  (aq) competes with S(IV) (aq) for the reaction with  $\text{OH}$ (aq),  $\text{O}_3$ , or  $\text{H}_2\text{O}_2$  (Table S1) (Ma et al., 2008). However, the  $\text{HONO}$  concentration becomes high at high  $\text{NO}_x$  lev-

els and enhances  $\text{SO}_2$  oxidation in the inorganic-salt seeded aqueous phase due to the formation of OH radicals via photolysis of  $\text{HONO}$ .

### 3.2 Heterogeneous oxidation in the presence of mineral dust particles

The heterogeneous chemistry in the presence of dust particles has been newly established in the AMAR model. The dust-phase module consists of a partitioning process (Sect. 3.2.1) and heterogeneous chemistry for  $\text{SO}_2$  and other trace gases (ozone,  $\text{HONO}$ , and  $\text{NO}_2$ ) (Table 3) (Fig. 1). The heterogeneous chemistry of  $\text{SO}_2$  is handled by autoxidation (Sect. 3.2.2) and photooxidation under UV light (Sect. 3.2.4). In dust-phase photochemistry, the central mechanism for  $\text{SO}_2$  oxidation is operated by the surface oxidants (e.g.,  $\text{OH}(\text{d})$ ), which is generated via the photoactivation process of semiconductive metal oxides in dust particles (Sect. 3.2.3).

#### 3.2.1 Gas–dust particle partitioning

In an adsorptive mode, water molecules suppress partitioning of  $\text{SO}_2$  because they compete for adsorptive sites with tracers (Cwiertny et al., 2008). However, the formation of the sulfate associated with ATD increased with increasing RH as shown in Table 1, suggesting that gas–dust partitioning is more likely operated by absorption on the multilayer coated dust with water molecules. ATD contains hygroscopic inorganic salts that form the thin water film on the surface of ATD particles when the salts are deliquescent (or above ERH). Some salts such as magnesium sulfate and calcium sulfate can be hydrated even at low humidity (Beardsley et al., 2013; Jang et al., 2010). Gustafsson et al. (2005) reported that ATD particles showed a substantially high affinity to water compared to pure  $\text{CaCO}_3$  particles. In their study, the water content of ATD particles, which was measured using the thermogravimetric method, ranged from two monolayers to four monolayers based on the BET surface area between 20 and 80 % relative humidity. This water layer influences gas–dust partitioning of atmospheric tracers such as  $\text{SO}_2$  and  $\text{NO}_2$ . The gas–dust partitioning constant ( $K_{\text{d},\text{SO}_2}$ ,  $\text{m}^3 \text{m}^{-2}$ ) of  $\text{SO}_2$  is defined as

$$K_{\text{d},\text{SO}_2} = \frac{[\text{SO}_2]_{\text{d}}}{[\text{SO}_2]_{\text{g}} A_{\text{Dust}}} \quad (\text{m}^3 \text{m}^{-2}), \quad (5)$$

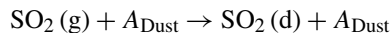
where  $A_{\text{dust}}$  ( $\text{m}^2 \text{m}^{-3}$ ) is the geometric surface concentration of ATD dust particles and is calculated by multiplying the dust mass concentration ( $\mu\text{g m}^{-3}$ ) by a geometric surface-mass ratio ( $f_{\text{dust,S\_M}}$ ) of ATD particles ( $3.066 \times 10^{-6}$ ,  $\text{m}^2 \mu\text{g}^{-1}$ ). The  $\text{SO}_2$  absorption and desorption processes for the dust phase are expressed as

**Table 3.** Dust-phase heterogeneous reactions and their rate constants in the presence of ATD particles.

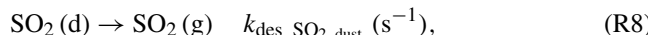
Reaction <sup>a</sup>	Rate constant <sup>b</sup>	Coefficients of rate constants <sup>b</sup>		$K_a^c$	Reference <sup>d</sup>	Note <sup>e</sup>
		$k_1$	$k_2$			
Partitioning						
1 $\text{SO}_2 + \text{Dust} \rightarrow \text{SO}_2(\text{d}) + \text{Dust}$	$k_{\text{abs}}$	$1 \times 10^{-8}$			AR05, HZ15	Reaction (R7)
2 $\text{SO}_2(\text{d}) \rightarrow \text{SO}_2$	$k_{\text{des}}$	$1 \times 10^9$	3100	0.013	AR05, HZ15	Reaction (R8)
3 $\text{O}_3 + \text{Dust} \rightarrow \text{O}_3(\text{d}) + \text{Dust}$	$k_{\text{abs}}$	$1 \times 10^{-8}$			MU03, US01	
4 $\text{O}_3(\text{d}) \rightarrow \text{O}_3$	$k_{\text{des}}$	$3 \times 10^{10}$	2700	0	MU03, US01	
5 $\text{NO}_2 + \text{Dust} \rightarrow \text{NO}_2(\text{d}) + \text{Dust}$	$k_{\text{abs}}$	$1 \times 10^{-8}$			CW84	
6 $\text{NO}_2(\text{d}) \rightarrow \text{NO}_2$	$k_{\text{des}}$	$1 \times 10^{10}$	2500	0	CW84	
7 $\text{HNO}_3 + \text{Dust} \rightarrow \text{HNO}_3(\text{d}) + \text{Dust}$	$k_{\text{abs}}$	$1 \times 10^{-8}$			SW81, Sc84	
8 $\text{HNO}_3(\text{d}) \rightarrow \text{HNO}_3$	$k_{\text{des}}$	$1 \times 10^{15}$	8700	15.4	SW81, Sc84	
9 $\text{HONO} + \text{Dust} \rightarrow \text{HONO}(\text{d}) + \text{Dust}$	$k_{\text{abs}}$	$1 \times 10^{-8}$			BK96	
10 $\text{HONO}(\text{d}) \rightarrow \text{HONO}$	$k_{\text{des}}$	$1 \times 10^{10}$	4900	0	BK96	
11 $\text{N}_2\text{O}_5 + \text{Dust} \rightarrow \text{HNO}_3(\text{d}) + \text{Dust}$	$k_{\text{abs}}$	$7.3 \times 10^{-3}$			WS09	
Dust phase						
1 $\text{Dust} + h\nu \rightarrow \text{Dust} + e\_h$	$k_{e\_h}^j$	$j_{[\text{ATD}]}$			Sect. 3.2.3	Reaction (R10)
2 $e\_h \rightarrow \text{energy}$	$k_{\text{recom}}$	$1 \times 10^{-2}$			Sect. 3.2.3	Reaction (R11)
3 $e\_h + \text{O}_2 \rightarrow \text{OH}(\text{d})$	$k_{\text{OH}, \text{O}_2}$	$1 \times 10^{-22}$	2.3RH		Sect. 3.2.3	Reaction (R12)
4 $\text{SO}_2(\text{d}) \rightarrow \text{SO}_4^{2-}(\text{d})$	$k_{\text{auto}}$	$5 \times 10^{-6}$			Sect. 3.2.2	Reaction (R9)
5 $\text{SO}_2(\text{d}) + \text{OH}(\text{d}) \rightarrow \text{SO}_4^{2-}(\text{d})$	$k_{\text{photo}}$	$1 \times 10^{-12}$			Sect. 3.2.4	Reaction (R13)
6 $\text{SO}_2(\text{d}) + \text{O}_3(\text{d}) \rightarrow \text{SO}_4^{2-}(\text{d}) + \text{O}_2$	$k_{\text{auto}, \text{O}_3}$	$2 \times 10^{-11}$			Sect. 3.3.1	Reaction (R14)
7 $e\_h + \text{O}_3(\text{d}) \rightarrow \text{OH}(\text{d}) + \text{O}_2$	$k_{\text{OH}, \text{O}_3}$	$1 \times 10^{-12}$			Sect. 3.3.1	Reaction (R15)
8 $\text{NO}_2(\text{d}) \rightarrow \text{NO}_3^-(\text{d})$	$k_{\text{auto}, \text{NO}_2}$	$6 \times 10^{-5}$			Sect. 3.3.2	Reaction (R18)
9 $e\_h + \text{NO}_2(\text{d}) \rightarrow \text{HONO}(\text{d})$	$k_{e\_h, \text{NO}_2}$	$6 \times 10^{-12}$			Sect. 3.3.2	Reaction (R16)
10 $\text{HONO}(\text{d}) + h\nu \rightarrow \text{OH}(\text{d}) + \text{NO}$	$k_{\text{HONO}}^j$	$j_{[\text{HONO} \rightarrow \text{OH}]}$			BK91, AB97	Reaction (R17)
11 $\text{NO}_2(\text{d}) + \text{OH}(\text{d}) \rightarrow \text{NO}_3^-(\text{d})$	$k_{\text{photo}, \text{NO}_2}$	$1 \times 10^{-10}$			Sect. 3.3.2	Reaction (R19)

<sup>a</sup> The unit of the chemical species (except dust) is molecule  $\text{cm}^{-3}$  for both partitioning process and dust-phase chemistry. The unit of the dust for model input is mass concentration ( $\mu\text{g m}^{-3}$ ) and is multiplied by a factor of  $2.45 \times 10^{10}$  for simulation. <sup>b</sup> The unit of reaction rate constants is  $\text{s}^{-1}$  for the first-order reactions and  $\text{cm}^3 \text{molecule}^{-1} \text{s}^{-1}$  for the second-order reactions.  $k_{\text{abs}}$  is uptake rate constant.  $k_{\text{abs}} = k_1 \omega f_{\text{dust}, \text{S\_M}}/4$ , where  $\omega = \sqrt{8RT/(\pi \text{MW})}$  ( $\text{m s}^{-1}$ ) and  $f_{\text{dust}, \text{S\_M}} = 3.066 \times 10^{-6}$  ( $\text{m}^2 \mu\text{g}^{-1}$ ).  $R$  is the ideal gas constant and  $\text{MW}$  ( $\text{g mol}^{-1}$ ) is the molecule weight of chemical species.  $k_{\text{des}}$  is desorption rate constant.  $k_{\text{des}} = k_1 \exp(-\frac{k_2}{F_{\text{water}}})/(F_{\text{water}}(1 + K_a/[\text{H}^+]))$ , where  $F_{\text{water}}$  is calculated using Eq. (8).  $[\text{H}^+]$  is dynamically calculated based on thermodynamic model (E-AIM II) (Clegg et al., 1998; Wexler and Clegg, 2002; Clegg and Wexler, 2011). The rate constants ( $k$ ) for dust-phase reactions is  $k = k_1 \exp(k_2)$ .  $k_{e\_h}^j$  and  $k_{\text{HONO}}^j$  are photocatalytic reaction rates. The cross sections and quantum yields of dust are estimated (see Sect. 2.2).

<sup>c</sup> Coefficient  $K_a$  is acid dissociation constant (see  $k_{\text{des}}$ ). <sup>d</sup> The rate constant parameters, which are noted as “this study”, are determined using the simulation of indoor chamber data (Park and Jang, 2016) (see Sect. 3). AB97, Atkinson et al. (1997); AR05, Adams et al. (2005); BK91, Bongartz et al. (1991); BK96, Becker et al. (1996); CW84, Chameides (1984); HZ15, Huang et al. (2015); MU03, Michel et al. (2003); Sc84, Schwartz (1984); SW81, Schwartz and White (1981); US01, Underwood et al. (2001); WS09, Wagner et al. (2009). <sup>e</sup> The reactions are noted with the numbers associated with the reaction in the main text.



$$k_{\text{abs, SO}_2, \text{dust}} \text{ (m}^3 \text{ m}^{-2} \text{ s}^{-1}\text{)}, \quad (R7)$$



where  $k_{\text{abs, SO}_2, \text{dust}}$  ( $\text{m}^3 \text{ m}^{-2} \text{ s}^{-1}$ ) and  $k_{\text{des, SO}_2, \text{dust}}$  ( $\text{s}^{-1}$ ) are the absorption rate constant and the desorption rate constant, respectively. At equilibrium, the absorption rate (R7) equals the desorption rate (R8). Thus,  $K_{\text{d, SO}_2}$  can be expressed as

$$K_{\text{d, SO}_2} = \frac{k_{\text{abs, SO}_2, \text{dust}}}{k_{\text{des, SO}_2, \text{dust}}} \text{ (m}^3 \text{ m}^{-2}\text{).} \quad (6)$$

The  $K_{\text{d, SO}_2}$  value at 20 % RH is set at  $1.63 \text{ (m}^3 \text{ m}^{-2}\text{)}$  based on the literature data (dust particles at 20 % RH) (Adams

et al., 2005; Huang et al., 2015). The characteristic time to reach to equilibrium is very short (Sect. 3.1.1). In kinetic mechanisms,  $k_{\text{ads, SO}_2, \text{dust}}$  was set at  $1.7 \times 10^3 \text{ m}^3 \text{ m}^{-2} \text{ s}^{-1}$  for dry particles (20 % RH) using the same approach as Eq. (2). The resulting characteristic time for  $k_{\text{ads, SO}_2, \text{dust}}$  is  $10^{-6} \text{ s}$ . The characteristic time of the reaction of  $\text{SO}_2$  with an  $\text{OH}$  radical ( $10^6 \text{ molecules cm}^{-3}$ ) is about  $10^6$ – $10^7 \text{ s}$  in gas phase and  $10^5$ – $10^6 \text{ s}$  in both aqueous phase and dust phase.

To consider the effect of temperature on  $K_{\text{d, SO}_2}$ , the temperature dependency of  $k_{\text{des, SO}_2, \text{dust}}$  (Eq. 6) is derived from the Henry's constant (Chameides, 1984).  $K_{\text{d, SO}_2}$  (Eq. 5) is also influenced by aerosol water content (Zuend et al., 2011) as well as the dissociation of  $\text{H}_2\text{SO}_3$ , which is operated by aerosol acidity ( $[\text{H}^+]$ ) and an acid dissociation constant ( $\text{K}_{\text{as, SO}_2}$ ) (Martell and Smith, 1976). Thus,  $k_{\text{des, SO}_2, \text{dust}}$  is ex-

pressed as

$$k_{\text{des-SO}_2, \text{dust}} = 1 \times 10^9 \exp\left(-\frac{3100}{T}\right) / \left(F_{\text{water}} \left(1 + \frac{K_{\text{d,SO}_2}}{[\text{H}^+]}\right)\right) \quad (7)$$

$K_{\text{d,SO}_2}$  is 0.013 (mol L<sup>-1</sup>) at 298 K (Martell and Smith, 1976). The influence of the dissociation of inorganic acid on  $K_{\text{d,SO}_2}$  is accounted for by the term  $(1 + \frac{K_{\text{d,SO}_2}}{[\text{H}^+]})$  in Eq. (7). The estimation of  $[\text{H}^+]$  is treated in the same ways as aqueous chemistry (Sect. 3.1.3).

In order to estimate  $K_{\text{d,SO}_2}$  at different RH,  $F_{\text{water}}$  (coefficient of the mass fraction of water to dust particles) was introduced into the model. The hygroscopic property of mineral dust dynamically changes because dust can be substantially modified by direct reaction of some of its components (e.g.,  $\text{CaCO}_3$ ) with inorganic acids such as  $\text{H}_2\text{SO}_4$  and  $\text{HNO}_3$ . When dust forms  $\text{Ca}(\text{NO}_3)_2$ , dust becomes more hygroscopic. Nitrate salts deliquesce at very low RH (17 %) (Krueger et al., 2003, 2004).  $\text{CaSO}_4$  is, however, relatively hydrophobic. Nitrate salts exist only when sulfate concentrations is very low. In the model,  $F_{\text{water}}$  is associated with the hygroscopic property of indigenous dust (first term in Eq. 8), the inorganic nitrates formed from the reaction of absorbed  $\text{HNO}_3$  with dust (second term), and the inorganic sulfate ( $\text{SO}_4^{2-}-\text{NH}_4^+-\text{H}_2\text{O}$  system, third term).

$$F_{\text{water}} = \exp(4.4 \text{RH}) + 3.7 f_{\text{dust,S\_M}} \exp(4.4 \text{RH}) \frac{[\text{NO}_3^-(\text{d\_salt})]}{A_{\text{Dust}}} + \frac{f_{\text{dust,S\_M}} M_{\text{in,water}}}{A_{\text{Dust}}}, \quad (8)$$

where  $M_{\text{in,water}}$  is the water concentration ( $\mu\text{g m}^{-3}$ ) associated with inorganic sulfate and calculated using E-AIM II. Both  $[\text{NO}_3^-(\text{d\_salt})]$  and  $M_{\text{in,water}}$  are normalized by the mass concentration of ATD particles ( $[\text{Dust}]$ ,  $\mu\text{g cm}^{-3}$ ).  $F_{\text{water}}$  is first determined using chamber simulation of  $\text{SO}_2$  heterogeneous oxidation (first and third terms in Eq. 8) (D1–D3 in Table 1) under varied RH levels and extended to  $\text{SO}_2$  oxidation in the presence of  $\text{NO}_x$  (Exp. 14 April 2017 in Table 2). Among temperature, RH, and aerosol acidity, the most influential variable is RH due to the variation in  $F_{\text{water}}$  (see sensitivity analysis in Sect. 5).

### 3.2.2 Autoxidation of $\text{SO}_2$ on dust surface

Typically, autoxidation of  $\text{SO}_2$  is an oxidation process via the reaction of absorbed  $\text{SO}_2$  (Reactions R7 and R8) with an oxygen molecule. In the model,  $[\text{SO}_4^{2-}]_{\text{auto}}$  is defined as the sulfate resulted from any oxidation reactions (autoxidation in open air and oxidation with ozone) of  $\text{SO}_2$  without UV light (Fig. 1). In autoxidation, the reaction of  $\text{SO}_2(\text{d})$  with the oxygen molecules is treated as the first-order reaction (assuming the concentration of oxygen is constant as  $2 \times 10^5$  ppm).

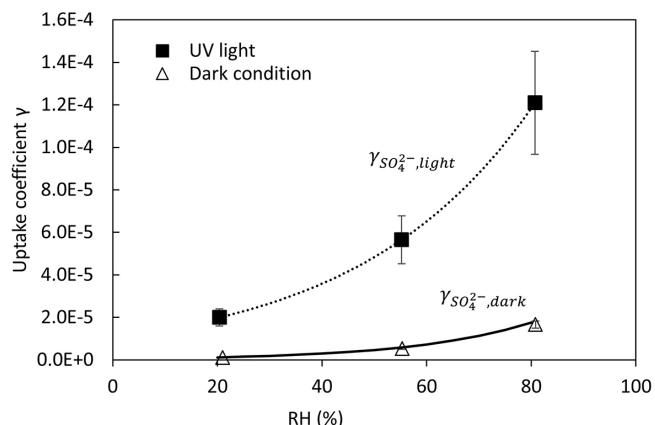
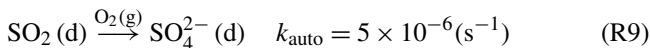


**Figure 2.** Uptake coefficient ( $\gamma$ ) of  $\text{SO}_2$  in the presence of the ATD particles under dark conditions and UV light conditions. The values of  $\gamma$  were obtained by kinetic model using indoor experimental data. The  $\gamma_{\text{SO}_4^{2-},\text{light}}$  is correlated to concentration of OH radicals and RH (%). The  $\gamma_{\text{SO}_4^{2-},\text{dark}}$  is a function of RH. The error bar of  $\gamma$  was derived from the model uncertainty.

Under dark conditions, the formation of sulfate is mainly sourced from autoxidation of  $\text{SO}_2$ . For comparison with other studies, we estimate the reactive uptake coefficient ( $\gamma_{\text{SO}_4^{2-},\text{auto}}$ ) of  $\text{SO}_2$  onto ATD dust in the absence of ozone and  $\text{NO}_x$  (Fig. 2).

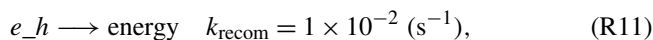
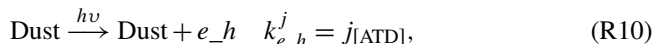
$$\gamma_{\text{SO}_4^{2-},\text{auto}} = \frac{4K_{\text{d,SO}_2}k_{\text{auto}}}{\omega_{\text{SO}_2}}, \quad (9)$$

$\gamma_{\text{SO}_4^{2-},\text{auto}}$  is proportional to  $K_{\text{d,SO}_2}$ , and influenced by humidity (Eq. 7).

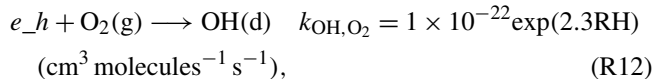
### 3.2.3 Photoactivation of dust particles and heterogeneous formation of OH radicals

The reactive uptake of  $\text{SO}_2$  on particles is traditionally treated as a first-order process (Ullerstam et al., 2003; Li et al., 2007). Such an approach is appropriate for simple autoxidation mechanisms, but not for the complex heterogeneous photooxidation of  $\text{SO}_2$ . In the AMAR model, the heterogeneous photooxidation of  $\text{SO}_2$  is approached in three steps: (1) the formation of an  $e_{\text{cb}}^- - h_{\text{vb}}^+$  pair via photoactivation of dust particles, (2) the formation of  $\text{OH}(\text{d})$  via the reaction of an  $e_{\text{cb}}^- - h_{\text{vb}}^+$  pair with a water or oxygen molecule, and (3) the reaction of absorbed  $\text{SO}_2$  with the resulting  $\text{OH}(\text{d})$  (second-order reactions) (Table S1).

The photoactivation of dust particles and the recombination reaction of an electron–hole pair ( $e_h$ ) are added into the model.



where  $k_{e_{-h}}^j$  is the photoactivation rate constant to form  $e_{\text{cb}}^- - h_{\text{vb}}^+$  pairs and  $k_{\text{recom}}$  is the reaction rate constant of recombination (heat radiation) of an electron and a hole. The value of  $k_{\text{recom}}$  is set at a large number to prevent the accumulation of electron–hole pairs. The formation of OH(d) is expressed as



where  $k_{\text{OH}, \text{O}_2}$  is the reaction rate constant to form OH(d) and is first estimated using indoor chamber data (L1–L3 in Table 1) at RH 20, 55, and 80 % and then regressed against RH. The study by Thiebaud et al. (2010) reported the recombination of OH(d) near to  $\text{TiO}_2$  surfaces. In our model, the mechanistic role of the catalytic formation of the electron–hole pairs (Reaction R10) and their recombination (Reaction R11) compensates the formation and the self-reaction of OH radicals.

In Reaction (R10),  $k_{e_{-h}}^j$  is the operational rate constant for the photoactivation of dust particles and is dependent on the photolysis rate constant,  $j_{[\text{ATD}]} \text{ (s}^{-1}\text{)}$ . Like the typical photolysis of a gaseous molecule, the photocatalytic production of  $e_{\text{cb}}^- - h_{\text{vb}}^+$  pairs is linear to both the actinic flux ( $I(\lambda)$ , photons  $\text{cm}^{-2} \text{ nm}^{-1} \text{ s}^{-1}$ ) originating from the light source and the photocatalytic property of dust particles. The value of  $j_{[\text{ATD}]}$  is determined by  $I(\lambda)$ , the absorption cross section ( $\sigma(\lambda)$ ,  $\text{cm}^2 \mu\text{g}^{-1}$ ), and the quantum yield ( $\phi(\lambda)$ ) of dust conducting matter at each wavelength range ( $\lambda$ , nm),

$$j_{[\text{ATD}]} = \int_{\lambda_1}^{\lambda_2} I(\lambda) \sigma(\lambda) \phi(\lambda) d\lambda. \quad (10)$$

In the model,  $\sigma(\lambda)$  is the light absorption needed to activate dust-phase semiconducting metal oxides (excitation from a ground energy level to a conducting band), and  $\phi(\lambda)$  is the probability of yielding the  $e_{\text{cb}}^- - h_{\text{vb}}^+$  pair in the dust phase. Both  $\sigma(\lambda)$  and  $\phi(\lambda)$  cannot be directly measured because of complexity in the quantity of photoactive conducting matter in dust particles and the irradiation processes of the  $e_{\text{cb}}^- - h_{\text{vb}}^+$  pair. In order to deal with  $\sigma(\lambda) \times \phi(\lambda)$ , we calculated the mass absorption cross section of dust particles ( $\text{MAC}_{\text{ATD}}$ ,  $\text{m}^2 \text{ g}^{-1}$ ), which was determined using the absorption coefficient of ATD particles ( $b_{\text{ATD}}$ ,  $\text{m}^{-1}$ ) with the particle concentration ( $m_{\text{ATD}}$ ,  $\text{g m}^{-3}$ ):

$$\text{MAC}_{\text{ATD}} = \frac{b_{\text{ATD}}}{m_{\text{ATD}}}. \quad (11)$$

In Eq. (11),  $b_{\text{ATD}}$  can be calculated from the absorbance of dust filter sample ( $\text{Abs}_{\text{ATD}}$ , dimensionless) measured using a

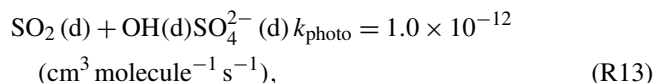
reflective UV–visible spectrometer (Fig. S3):

$$b_{\text{ATD}} = \frac{\text{Abs}_{\text{ATD}} A}{f V} \ln, \quad (12)$$

where  $A = 7.85 \times 10^{-5} \text{ (m}^2\text{)}$  is the sampled area on the filter and  $V (\text{m}^3)$  is the total air volume passing through the filter during sampling. In order to eliminate the absorbance caused by filter material scattering, a correction factor ( $f = 1.4845$ ) is obtained from a previous study (Zhong and Jang, 2011) and coupled into Eq. (12). The preliminary study showed that the effect of aerosol scattering on the  $b_{\text{abs}}$  values of the aerosol collected on the filter was negligible. Further, Bond (2001) reported that particle light scattering does not significantly influence spectral absorption selectivity. The  $\text{MAC}_{\text{ATD}}$  of dust particles originates from photocatalytic conducting matter (e.g.,  $\text{TiO}_2$ ) as well as light-absorbing matter (e.g., gypsum and metal sulfate). Thus, the  $\text{MAC}_{\text{ATD}}$  spectrum is adjusted using the known  $\text{TiO}_2$  absorption spectrum (Reyes-Coronado et al., 2008) and applied to  $\sigma(\lambda) \times \phi(\lambda)$  (Fig. S3). The resulting  $\sigma(\lambda) \times \phi(\lambda)$  spectrum is applied to Eq. (10) to calculate  $j_{[\text{ATD}]}$  (Reaction R10).

### 3.2.4 Heterogeneous photooxidation of $\text{SO}_2$

$\text{SO}_2$  is oxidized by OH(d) on the surface of ATD particles as follows:



where  $k_{\text{photo}}$  is the reaction rate constant of  $\text{SO}_2$  with OH(d) and is estimated from gas-phase Reaction (R1). Combining Eq. (4), (5), Reactions (R11) and (R15), the reactive uptake coefficient ( $\gamma_{\text{SO}_4^{2-}, \text{photo}}$ ) of  $\text{SO}_2$  on ATD particles under UV light can be written as

$$\gamma_{\text{SO}_4^{2-}, \text{photo}} = \frac{4K_{\text{d}, \text{SO}_2} (k_{\text{photo}} [\text{OH}(\text{d})] + k_{\text{auto}})}{\omega_{\text{SO}_2}}, \quad (13)$$

where  $\gamma_{\text{SO}_4^{2-}, \text{photo}}$  is the constant at a given concentration of OH(d) (for a given light source, dust concentration, and humidity) (Reactions R10 and R12). Figure 2 illustrates  $\gamma_{\text{SO}_4^{2-}, \text{photo}}$  values at three different RHs, which were obtained using indoor chamber data.  $\gamma_{\text{SO}_4^{2-}, \text{photo}}$  is significantly influenced by both UV light and humidity. For example,  $\gamma_{\text{SO}_4^{2-}, \text{photo}}$  is 1 order of magnitude higher than  $\gamma_{\text{SO}_4^{2-}, \text{auto}}$  at low  $\text{NO}_x$  levels (< 5 ppb), and  $\gamma_{\text{SO}_4^{2-}, \text{photo}}$  increased from  $2.0 \times 10^{-5}$  to  $1.24 \times 10^{-4}$  when the RH changed from 20 to 80 %.

### 3.3 Impact of ozone and $\text{NO}_x$ on heterogeneous chemistry of $\text{SO}_2$

To date, most studies of the effect of  $\text{NO}_x$  on sulfate formation have been limited to the reaction under dark conditions.

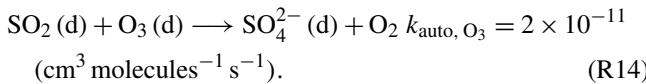
For example, previous laboratory studies using pure metal oxides reported the acceleration of the heterogeneous oxidation of  $\text{SO}_2$  by  $\text{NO}_x$  under dark conditions (Ma et al., 2008; Liu et al., 2012). For the effect of ozone, the recent chamber study by Park and Jang (2016) showed significant enhancement of heterogeneous photooxidation of  $\text{SO}_2$ . In the AMAR model, the formation of sulfate is also modulated by the involvement of ozone and  $\text{NO}_x$  in both autoxidation and photochemistry on the surface of dust particles (Fig. 1).

### 3.3.1 Dust-phase ozone chemistry

The gas–dust partitioning coefficient of ozone is scaled using  $K_{\text{d},\text{SO}_2}$  and the ratio of the Henry's law constant of  $\text{SO}_2$  ( $K_{\text{H},\text{SO}_2}$ , Eq. 1) to that of ozone ( $K_{\text{H},\text{O}_3} = 1.2 \times 10^{-2} \text{ mol L}^{-1} \text{ atm}^{-1}$  at 298 K) (Chameides, 1984),

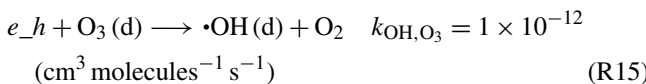
$$K_{\text{d},\text{O}_3} = K_{\text{d},\text{SO}_2} \frac{K_{\text{H},\text{O}_3}}{K_{\text{H},\text{SO}_2}} = 7.7 \times 10^{-7} F_{\text{water}} \exp\left(\frac{2700}{T}\right) (\text{m}^3 \text{ m}^{-2}). \quad (14)$$

The partitioning process is also treated by the absorption–desorption kinetic mechanism as shown in Reactions (R7) and (R8) (Table 3: partitioning). Ozone can decay catalytically in the dust phase, forming an oxygen molecule and surface-bound atomic oxygen (Usher et al., 2003; Chang et al., 2005). The formed atomic oxygen reacts with  $\text{SO}_2(\text{d})$  to form sulfate (Ullerstam et al., 2002; Usher et al., 2002):



In the presence of  $300 \mu\text{g m}^{-3}$  of ATD particles and 60 ppb of ozone, the concentration of  $\text{O}_3(\text{d})$  is estimated as  $2.4 \times 10^7 \text{ molecule cm}^{-3}$ . Under this condition, the characteristic time of the autoxidation by ozone (Reaction R14) is  $2 \times 10^3 \text{ s}$  and is much faster than the autoxidation by oxygen (Reaction R9,  $2 \times 10^5 \text{ s}$ ). At nighttime, in the presence of ozone, the autoxidation of  $\text{SO}_2(\text{d})$  yields a significant amount of sulfate.

Under UV light, ozone is also involved in the production of the surface oxidants ( $\text{O}_3^-$ ,  $\text{HO}_3$  radicals, and  $\text{OH}$  radicals) that further promote heterogeneous oxidation of  $\text{SO}_2$ .  $\text{O}_3(\text{d})$  acts as an acceptor for  $e_{\text{cb}}^- - h_{\text{vb}}^+$  and forms  $\text{OH}(\text{d})$ .



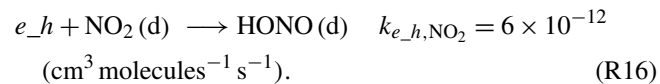
### 3.3.2 Dust-phase $\text{NO}_x$ chemistry

The gas–dust partitioning coefficient of  $\text{NO}_2$  ( $K_{\text{d},\text{NO}_2}$ ) is treated as the same approach with ozone, using  $K_{\text{d},\text{SO}_2}$  and the ratio of  $K_{\text{H},\text{SO}_2}$  (Eq. 1) to the Henry's law constant of  $\text{NO}_2$  ( $K_{\text{H},\text{NO}_2} = 1.2 \times 10^{-2} \text{ mol L}^{-1} \text{ atm}^{-1}$  at

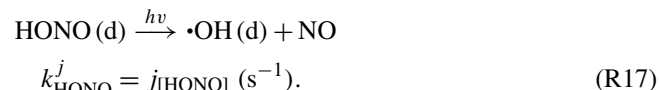
298 K) (Chameides, 1984).

$$K_{\text{d},\text{NO}_2} = K_{\text{d},\text{SO}_2} \frac{K_{\text{H},\text{NO}_2}}{K_{\text{H},\text{SO}_2}} = 1.5 \times 10^{-6} F_{\text{water}} \exp\left(\frac{2500}{T}\right) (\text{m}^3 \text{ m}^{-2}) \quad (15)$$

The absorbed  $\text{NO}_2$  first reacts with  $e_{\text{cb}}^-$  (d) or  $\cdot\text{O}_2^-$  (d) on the dust surface (Reaction R10) and forms  $\text{HONO}(\text{d})$  (Ma et al., 2008; Liu et al., 2012; Saliba and Chamseddine, 2012; Saliba et al., 2014). In AMAR, the formation of  $\text{HONO}(\text{d})$  is simplified into



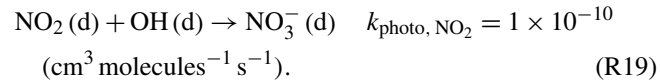
$\text{HONO}(\text{d})$  is further decomposed through photolysis and yields  $\text{OH}(\text{d})$ :



The photolysis rate constant of  $\text{HONO}(\text{d})$  is treated with the one for gaseous  $\text{HONO}$  ( $j_{[\text{HONO}]}$ ). Similar to autoxidation of  $\text{SO}_2$  (Sect. 3.2.2),  $\text{NO}_2(\text{d})$  autoxidizes to form nitrate:



$\text{NO}_2$  reacts with  $\text{OH}(\text{d})$ :



$k_{\text{auto}, \text{NO}_2}$  and  $k_{\text{photo}, \text{NO}_2}$  was determined using the simulation of outdoor chamber data (Exp. 14 April 2017 in Table 2). The estimation of the gas–dust partitioning coefficients of  $\text{HONO}$  ( $K_{\text{d},\text{HONO}}$ ) (Becker et al., 1996) and  $\text{HNO}_3$  ( $K_{\text{d},\text{HNO}_3}$ ) (Schwartz and White, 1981) was approached using the similar method for  $\text{SO}_2$  (Table 3).  $\text{N}_2\text{O}_5$  forms nitrate via a reactive uptake process as shown in Table 3 (partitioning Reaction 11).

## 4 Simulation of the AMAR model

At the beginning of the development of the AMAR model, the kinetic parameters to predict the formation of sulfate and nitrate in the presence of ATD particles were leveraged using an indoor chamber. In order to test the feasibility of the resulting AMAR model, the UF-APHOR data using natural sunlight were simulated (Table 2). The chamber dilution (measured by  $\text{CCl}_4$ ) and the wall process of gaseous compounds (e.g., ozone,  $\text{SO}_2$ ,  $\text{HONO}$ ,  $\text{NO}_2$ ) and particles were integrated with the kinetic mechanisms to simulate UF-APHOR data (Sect. S1). As shown in Fig. 1, the model inputs are the concentration of chemical species, the amount of dust, and the meteorological variables that are commonly found at regional scales. The dual chambers allow for two controlled experiments to be performed simultaneously under the same meteorological conditions.

#### 4.1 Simulations for different dust loadings

Figure 3 shows that the predicted  $[\text{SO}_4^{2-}]_T$  is in good agreement with experimental observations, which were performed under low- $\text{NO}_x$  conditions ( $\text{NO}_x < 5 \text{ ppb}$ ) for two different dust loadings as well as two different  $\text{SO}_2$  levels. The greater increase in  $[\text{SO}_4^{2-}]_T$  appeared with the higher sunlight intensity (between 11:00 and 14:00). In Fig. 3a, the predicted  $[\text{SO}_4^{2-}]_T$  increased by 63 % (at 3 PM) with  $290 \mu\text{g m}^{-3}$  of ATD particles compared to the  $[\text{SO}_4^{2-}]_T$  without dust particles. Figure 3b confirms that the larger dust particle loading yields more  $[\text{SO}_4^{2-}]_T$ . In Fig. 3c,  $[\text{SO}_4^{2-}]_T$  was predicted with high and low initial concentrations of  $\text{SO}_2$  for a given dust loading. The time profiles of the simulation of concentrations of  $\text{NO}_x$ , ozone,  $\text{SO}_2$ , and dust are shown in Fig. S4.

Because of the large size of dust particles, the wall processes (e.g., settling and wall deposition) of dust particles is greater than that of the sulfate particles originated from  $[\text{SO}_4^{2-}]_{\text{aq}}$  (no dust). Hence, the fraction of  $[\text{SO}_4^{2-}]_{\text{dust}}$  to  $[\text{SO}_4^{2-}]_T$  declines over the course of the chamber experiment. To estimate how the predicted  $[\text{SO}_4^{2-}]_T$  is attributed to  $[\text{SO}_4^{2-}]_{\text{aq}} + [\text{SO}_4^{2-}]_{\text{gas}}$  (non-dust sulfate) and  $[\text{SO}_4^{2-}]_{\text{dust}}$  without wall processes, Fig. 3d, e, and f are reconstructed from Fig. 3a, b, and c, respectively. As shown in the inner pie chart of Fig. 3d, a significant fraction of  $[\text{SO}_4^{2-}]_T$  is attributed to dust-phase chemistry ( $[\text{SO}_4^{2-}]_{\text{auto}} + [\text{SO}_4^{2-}]_{\text{photo}}$ : 0.58). In Fig. 3e, the fraction of final  $[\text{SO}_4^{2-}]_{\text{photo}}$  to  $[\text{SO}_4^{2-}]_T$  increases from 0.28 to 0.72 with the increase in dust loading from 90 to  $403 \mu\text{g m}^{-3}$ . The increased dust loading promotes both the absorption of  $\text{SO}_2$  onto dust particles and the production of dust-phase oxidants and thus yields more sulfate production. With the increase in the initial concentration of  $\text{SO}_2$  from 119 to  $272 \text{ ppb}$  in Fig. 3f, the fraction of  $[\text{SO}_4^{2-}]_{\text{photo}}$  and  $[\text{SO}_4^{2-}]_{\text{gas}} + [\text{SO}_4^{2-}]_{\text{aq}}$  are not much changed, while  $[\text{SO}_4^{2-}]_T$  increases from  $16.6$  to  $30.1 \mu\text{g m}^{-3}$ . The elevation of the concentration of  $\text{SO}_2$  produces more sulfate in all three phases (gas, aqueous, and dust phases). The sulfuric acid formed in the aqueous phase is hydrophilic and creates a positive feedback loop which aggravates the growth of aqueous aerosol. Overall, the variation in dust concentration is more influential on  $[\text{SO}_4^{2-}]_{\text{photo}}$  than that of  $\text{SO}_2$ .

#### 4.2 Simulation of $\text{NO}_x$ effect

Figure 4 shows that the model performs well in predicting  $[\text{SO}_4^{2-}]_T$  in various levels of  $\text{NO}_x$ . Figure 4d is reconstructed from Fig. 4a, b, and c to illustrate how  $[\text{SO}_4^{2-}]_T$  is attributed to the aqueous-phase reaction ( $[\text{SO}_4^{2-}]_{\text{gas}} + [\text{SO}_4^{2-}]_{\text{aq}}$ ), dust-phase autoxidation ( $[\text{SO}_4^{2-}]_{\text{auto}}$ ), and dust photochemistry ( $[\text{SO}_4^{2-}]_{\text{photo}}$ ). Comparing Fig. 4b with c,  $[\text{SO}_4^{2-}]_{\text{photo}}$  is suppressed at high  $\text{NO}_x$  levels because  $\text{NO}_2$  competes for the consumption of dust-phase OH radicals with  $\text{SO}_2$ . The reduction of  $[\text{SO}_4^{2-}]_T$  in the afternoon is due to the particle loss

at the low concentrations of  $\text{SO}_2$ . The simulated concentrations of  $\text{NO}_x$ , ozone,  $\text{SO}_2$ , and dust are shown in Fig. S5.

The time profiles of the predicted  $[\text{NO}_3^-]_T$  are also shown in Fig. 4a, b, and c. In the morning,  $\text{NO}_2$  quickly oxidizes to accumulate nitric acid in the dust phase. The dust-phase nitric acid might rapidly react with alkaline carbonates (e.g., K, Na, Ca and Mg ions) in the dust phase and form nitrate salts ( $\text{NO}_3^- (\text{d}_\text{salt})$ ) in Reaction S23 of dust-phase reactions in Table S1). As described in Sect. 3.2.1, these nitrate salts are very hygroscopic and further enhance gas–dust partitioning of gaseous species including  $\text{HNO}_3$ ,  $\text{SO}_2$ , and  $\text{HONO}$  at high humidity (in the morning). With increasing sunlight intensity, the temperature increases but humidity decreases (20 %, Fig. S6) and thus increase the desorption of  $\text{HNO}_3$ . In addition to meteorological conditions, the formation of low-volatility sulfuric acid can deplete nitrate via evaporation of volatile nitric acid ( $\text{NO}_3^- (\text{d}_\text{salt})$ ) in Reactions S24 and S25 of dust-phase reactions in Table S1) from the dust surface. The capacity of ATD particles to form nitrate salts (or sulfate salts) is limited by the amount of carbonates and metal oxides on the surface of dust particles. This capacity is estimated to be 0.6 ppb (the number concentration of reactive sites in air), which was determined by comparing the actual aerosol acidity, as measured by colorimetry integrated with a reflectance UV–visible spectrometer (C-RUV), to the aerosol acidity predicted by the inorganic thermodynamic model (E-AIM II) using the inorganic composition from PILS-IC (Li et al., 2015; Beardsley and Jang, 2016). As shown in Fig. 4, the effect of  $\text{HNO}_3$  on the heterogeneous reaction is negligible during the daytime because sulfuric acid, a strong acid, depletes partitioning of  $\text{HNO}_3$  (Eq. 15). At the end of the photooxidation, nitrate is slightly underestimated because some observed nitrate may be trapped under the layer of hydrophobic alkaline sulfate formed via aging of ATD particles (effloresced). The surface  $\text{HONO}(\text{d})$ , which formed via the photocatalytic process of  $\text{NO}_2$  (Reaction R16), can influence the production of  $\text{OH}(\text{d})$ . However, the model analysis originated from the integrated reaction rate (IRR), an accumulated flux of chemical formation, suggests that the contribution of  $\text{HONO}(\text{d})$  to  $\text{OH}(\text{d})$  production is relatively small compared to the direct photocatalytic process caused by dust particles shown in Sect. 3.2.3.

#### 5 Sensitivity and uncertainties

The sensitivity of sulfate prediction to major variables (e.g., temperature, humidity, sunlight profile, the concentration of  $\text{SO}_2$  and  $\text{NO}_x$ , and dust loading) is illustrated in Fig. 5. To avoid the suppression of dust chemistry at high  $\text{NO}_x$  levels, the most sensitivity tests were performed at low levels of  $\text{NO}_x$ . The stacked chart normalized with  $[\text{SO}_4^{2-}]$  in Fig. 5 shows how  $[\text{SO}_4^{2-}]_T$  is attributed to  $[\text{SO}_4^{2-}]_{\text{auto}}$ ,  $[\text{SO}_4^{2-}]_{\text{photo}}$  and  $[\text{SO}_4^{2-}]_{\text{aq}} + [\text{SO}_4^{2-}]_{\text{gas}}$  (non-dust chemistry).

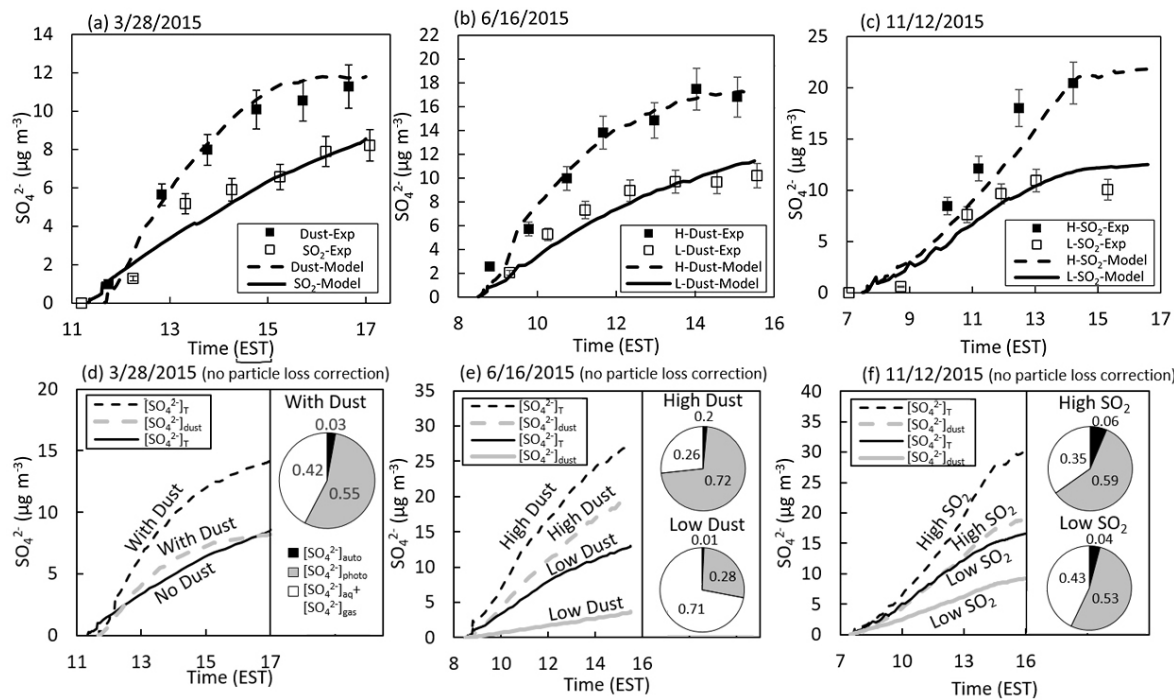


**Figure 3.** Time profiles of total sulfate concentration ( $\text{SO}_4^{2-}$ ,  $\mu\text{g m}^{-3}$ ) in the UF-APHOR. “Exp” denotes the experimentally observed sulfate ( $[\text{SO}_4^{2-}]_T$ ) and “Model” denotes the model-predicted sulfate. “H” and “L” represent the high and the low initial concentrations of chemical species. The errors associated with the concentration of sulfate is  $\pm 10\%$  originated from the PILS-IC measurement. **(a)** Sulfate formation with and without ATD particles ( $\text{SO}_2$  60 ppb vs.  $\text{SO}_2$  56 ppb and dust  $290 \mu\text{g m}^{-3}$ ). **(b)** The high and low loadings of dust particles (dust  $90 \mu\text{g m}^{-3}$  and  $\text{SO}_2$  100 ppb vs. dust  $404 \mu\text{g m}^{-3}$  and  $\text{SO}_2$  120 ppb). **(c)** The high and the low concentrations of  $\text{SO}_2$  ( $\text{SO}_2$  119 ppb and dust  $239 \mu\text{g m}^{-3}$  vs.  $\text{SO}_2$  272 ppb and dust  $230 \mu\text{g m}^{-3}$ ). For **(a)**, **(b)**, and **(c)**, the simulations included the chamber dilution and the wall process of gaseous compounds and particles (Sect. S1). For **(d)**, **(e)**, and **(f)**, the wall process for the particle loss was excluded to estimate the influence of ATD particles on sulfate formation without the chamber artifacts. In **(d)**, **(e)**, and **(f)**, total sulfate was decoupled into the sulfate originated from dust chemistry ( $[\text{SO}_4^{2-}]_{\text{dust}} = [\text{SO}_4^{2-}]_{\text{photo}} + [\text{SO}_4^{2-}]_{\text{auto}}$ ). The pie charts inserted into **(d)**, **(e)**, and **(f)** illustrate how total sulfate is attributed to major pathways at the end of the experiments.

Figure 5a illustrates that the reduction of  $[\text{SO}_4^{2-}]_T$  at a higher temperature (273 vs. 298 K) is ascribed to the decrease in the partitioning process. Figure 5b shows that  $[\text{SO}_4^{2-}]_T$  increases by a factor of 2.8 with RH increasing from 25 to 80 %. Humidity plays an important role in the modulation of both aerosol acidity and liquid water content, and ultimately influences the partitioning process (e.g.,  $\text{SO}_2$  partitioning on dust surface) and dust-phase chemistry (e.g., production of OH(d)). In the stacked column chart of Fig. 5b, the contribution of  $[\text{SO}_4^{2-}]_{\text{dust}}$  to  $[\text{SO}_4^{2-}]_T$  increases from 0.73 to 0.86 with increasing RH, suggesting that dust chemistry is more sensitive to humidity than aqueous-phase chemistry. Figure 5c presents  $[\text{SO}_4^{2-}]_T$  at two different sunlight intensities (winter on 12 November 2015 vs. summer on 25 April 2017) in Gainesville, Florida (latitude/longitude:  $29.64185^\circ/ -82.347883^\circ$ ). As shown in Fig. 5d, with  $\text{SO}_2$  concentrations increasing from 20 to 100 ppb,  $[\text{SO}_4^{2-}]_T$  increases by a factor of 4.4 in the given simulation condition. The effect of the concentration of  $\text{SO}_2$  on  $[\text{SO}_4^{2-}]_T$  has been discussed in Sect. 4.1 above. Figure 5e shows the

sensitivity of  $[\text{SO}_4^{2-}]_T$  to the ATD loading (100, 200, and  $400 \mu\text{g m}^{-3}$ ). With the increasing of dust loading, the contribution of  $[\text{SO}_4^{2-}]_{\text{photo}}$  to  $[\text{SO}_4^{2-}]_T$  also increases. Figure 5f illustrates how sulfate formation is suppressed by different  $\text{NO}_x$  levels (also see Sect. 3.3.2).

The inorganic thermodynamic model (E-AIM II) was employed to estimate  $[\text{H}^+]$  and the liquid water content ( $M_{\text{in,water}}$ ) for the  $\text{SO}_4^{2-}-\text{NH}_4^+-\text{H}_2\text{O}$  system (excluding  $\text{SO}_4^{2-}(\text{d}_{\text{salt}})$  in Reaction 13 of Table 3: dust phase) (Eq. 8) in both inorganic-salt seeded aqueous-phase and dust-phase chemistry. The uncertainty in  $M_{\text{in,water}}$  and  $[\text{H}^+]$  influences the partitioning tracers and consequently causes the uncertainty in  $[\text{SO}_4^{2-}]_T$ . The uncertainties in the prediction of  $[\text{H}^+]$  using inorganic thermodynamic models are large because of the limited data (Clegg et al., 1998; Wexler and Clegg, 2002). In this study,  $[\text{H}^+]$  is estimated by E-AIM II (Clegg et al., 1998; Wexler and Clegg, 2002; Clegg and Wexler, 2011) and corrected for the ammonia-rich condition (Li et al., 2015; Li and Jang, 2012). The reported uncertainty in  $[\text{H}^+]$  associated with the C-RUV method is  $\pm 18\%$ . Figure S7 illustrates the

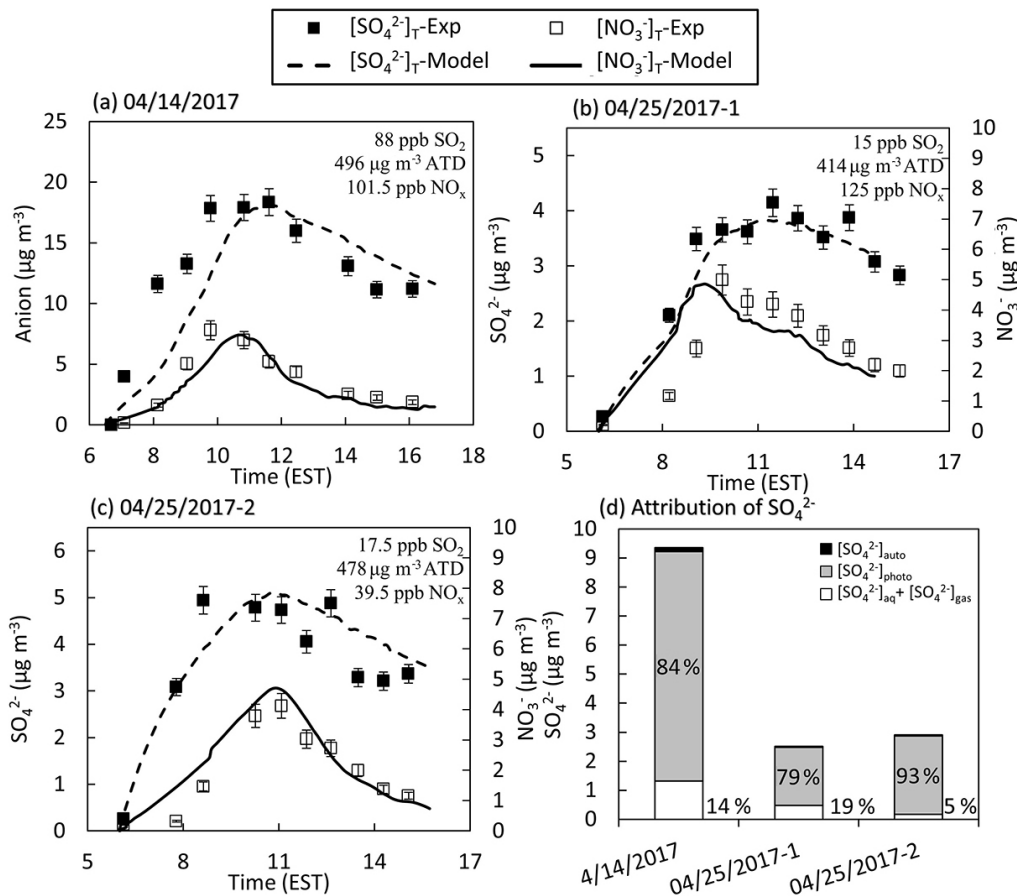


**Figure 4.** Time profiles of total sulfate concentration ( $[SO_4^{2-}]_T$ ,  $\mu\text{g m}^{-3}$ ) and nitrate concentration ( $[NO_3^-]_T$ ,  $\mu\text{g m}^{-3}$ ) in the dual-chamber experiments using UF-APHOR at different  $NO_x$  levels. The concentrations of sulfate and nitrate were measured using PILS-IC during the experiments. The error bars of the concentration of sulfate and nitrate is  $\pm 10\%$  originated from the PILS-IC measurement. The detailed experimental conditions of (a), (b), and (c) are shown in Table 2. Panel (d) shows how total sulfate is attributed to aqueous-phase reaction (sulfate formation in gas phase + sulfate formation in inorganic salted inorganic aqueous phase) ( $[SO_4^{2-}]_{\text{aq}} + [SO_4^{2-}]_{\text{gas}}$ ), dust-phase autoxidation ( $[SO_4^{2-}]_{\text{auto}}$ ), and dust photochemistry ( $[SO_4^{2-}]_{\text{photo}}$ ) at the end of the experiments. “Exp” denotes the experimental observation and “Model” denotes the simulation using the AMAR module. The chamber dilution and the wall process of gaseous compounds and particles were included in the simulation (Sect. S1).

uncertainties of the major model parameters ( $[H^+]$ ,  $F_{\text{water}}$ ,  $K_{d,SO_2}$ ,  $k_{\text{auto}}$  and  $k_{OH, O_2}$ ) and the prediction of  $[SO_4^{2-}]_T$ . The uncertainty in  $F_{\text{water}}$  ranges from  $-20$  to  $30\%$  due to the uncertainty in the measurement of sulfate ( $\pm 10\%$ ) and ammonia ions ( $\pm 10\%$ ) using PILS-IC. The propagation error in Eqs. (6) and (7) is used to estimate the uncertainty in  $K_{d,SO_2}$  ( $-20$  to  $30\%$ ). The uncertainty in  $k_{\text{auto}}$  ( $-48$  to  $42\%$ ) and  $k_{OH, O_2}$  ( $-20$  to  $22\%$ ) are estimated by simulating  $[SO_4^{2-}]_T$  within the uncertainty in  $K_{d,SO_2}$  and the measurement of sulfate ( $\pm 10\%$ ). The uncertainty in  $[SO_4^{2-}]_T$  was estimated to be  $\pm 12\%$  at the end of the simulation. In this model, the Henry’s law constant that is applied to gas–dust partitioning of tracers (Sect. 3.2.1) may lead to some biases in the prediction of sulfate or nitrate.

## 6 Conclusion and atmospheric implication

The AMAR model of this study was developed to predict the oxidation of  $SO_2$  and  $NO_x$  using comprehensive kinetic mechanisms in the gas phase, inorganic seeded aqueous phase, and dust phase. The thermodynamic parameters engaged in the partitioning process between gas, inorganic salted aqueous aerosol, and dust phases were obtained from known data in the literature (Table 3), and the kinetic parameters for dust chemistry were estimated using previously reported indoor chamber data (Park and Jang, 2016). Overall, the AMAR simulations were consistent with experimentally observed outdoor chamber data (Figs. 3 and 4) under ambient sunlight. As discussed in the sensitivity analysis (Sect. 5), both the  $[SO_4^{2-}]_T$  and the relative distribution of mechanism-based sulfate formation are sensitive to all major variables

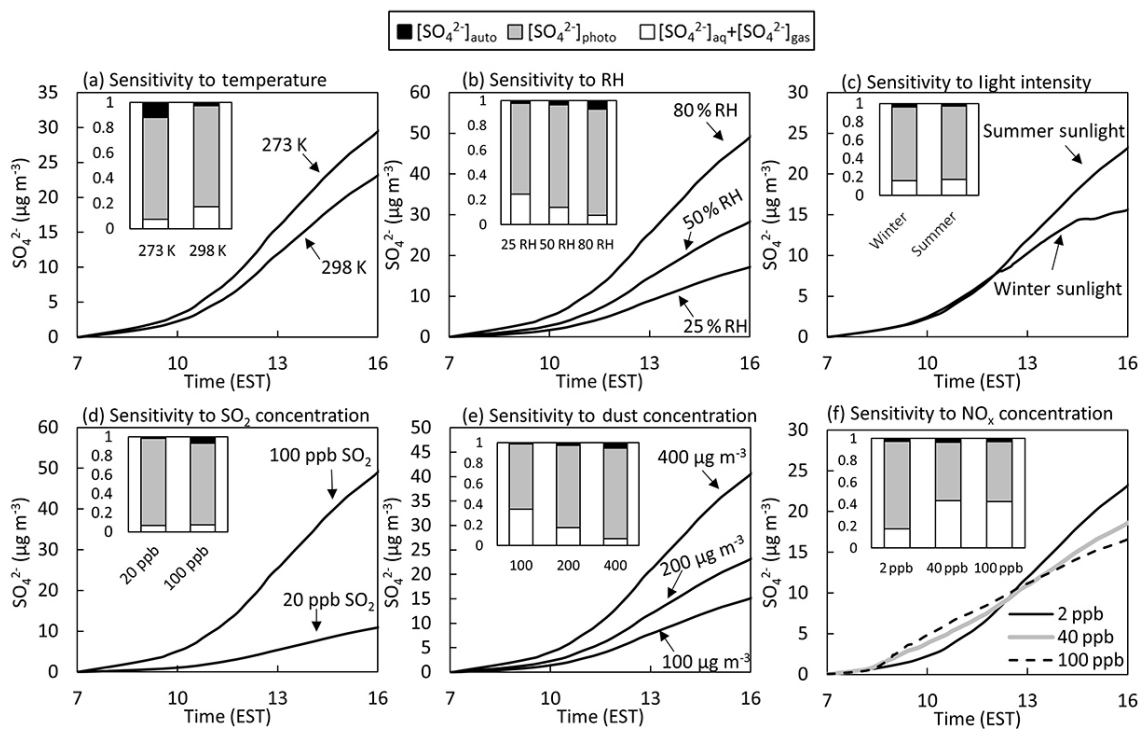


**Figure 5.** Sensitivity test of AMAR model to (a) temperature at 273 and 298 K; (b) RH at 25, 50, and 80 %; (c) sunlight profiles of summertime (25 April 2017) and wintertime (12 November 2015) at Gainesville, Florida (latitude/longitude:  $29.64185^\circ$ – $-82.347883^\circ$ ); (d) the concentration of  $\text{SO}_2$ ; (e) the concentration of dust particles; and (f) the  $\text{NO}_x$  concentration (initial  $\text{NO} : \text{NO}_2 = 1 : 1$ ). The stacked column chart in each figure illustrates how total sulfate is attributed to major pathways at the end of each experiment. For the sensitivity test, the chamber simulation is conducted with 100 ppb of initial  $\text{SO}_2$ , 2 ppb of initial  $\text{NO}_2$ , 2 ppb of initial  $\text{O}_3$ , and  $200 \mu\text{g m}^{-3}$  of ATD particles at  $T = 298 \text{ K}$  and  $\text{RH} = 40\%$  under ambient sunlight on 25 April 2017.  $\text{NO}_x$  (rate of flux =  $2.7 \times 10^6, \text{s}^{-1}$ ) and isoprene (rate of flux =  $2.7 \times 10^6, \text{s}^{-1}$ ) were constantly added to simulate chamber dilution. The simulation was performed without considering the particle loss to the chamber wall.

(model inputs), including temperature, humidity, sunlight intensity, the quantity of dust loading, and concentrations of  $\text{NO}_x$  and  $\text{SO}_2$ .

In order to assess the importance of dust chemistry in ambient conditions, the prediction of sulfate formation in the presence of ATD dust needs to be extended to 24 h simulations under various environmental conditions. Figure S8 shows the output simulated for 24 h with  $200 \mu\text{g m}^{-3}$  of ATD particle loading under urban (40 ppb  $\text{NO}_x$ ;  $\text{VOC} / \text{NO}_x < 5$ ; 20 ppb  $\text{SO}_2$ ) and rural atmospheres (5 ppb  $\text{NO}_x$ ;  $\text{VOC} / \text{NO}_x > 20$ ; 2 ppb  $\text{SO}_2$ ). At nighttime, when the temperature drops and humidity increases (70–90 %, Fig. S6), the contribution of  $[\text{SO}_4^{2-}]_{\text{auto}}$  to  $[\text{SO}_4^{2-}]_T$  becomes larger than the typical chamber simulation during the daytime. In a rural environment,  $[\text{SO}_4^{2-}]_{\text{photo}}$  is still the most influential on sulfate formation (0.76 fraction of  $[\text{SO}_4^{2-}]_T$  in Fig. S8a). For the simulation in a polluted area (Fig. S8b), the fraction of  $[\text{SO}_4^{2-}]_{\text{photo}}$  to  $[\text{SO}_4^{2-}]_T$  significantly decreases (0.61) because of the suppression induced by  $\text{NO}_x$  (Sect. 3.3.2), but the fraction of  $[\text{SO}_4^{2-}]_{\text{auto}}$  to  $[\text{SO}_4^{2-}]_T$  increases (0.28). With decreasing sunlight intensity

(after 5 PM), Fig. S8 shows the rapid increases in  $[\text{SO}_4^{2-}]_{\text{auto}}$  due to the reaction of dust-phase  $\text{SO}_2$  with ozone, which is the result of daytime photooxidation (Sect. 3.3.1). Figure S8 suggests that the failure to predict sulfate formation without accurate dust chemistry ( $[\text{SO}_4^{2-}]_{\text{auto}} + [\text{SO}_4^{2-}]_{\text{photo}}$ ) can lead to substantial underestimation of the quantity of total sulfate at regional or global scales.  $\text{SO}_2$  autoxidation alone may partially improve the prediction of sulfate in the presence of mineral dust, but sulfate production can still be largely underestimated and incorrectly predicted in time series when heterogeneous photocatalytic reactions in kinetic mechanisms are not considered.

The ATD particles in this study have chemical and physical properties different from ambient mineral dust particles. In general, the uptake coefficient of  $\text{SO}_2$  in authentic mineral dust particles (e.g., Gobi Desert dust and Saharan dust) is known to be higher than that of ATD particles (Crowley et al., 2010). Thus, the effect of ambient dust particles on heterogeneous photocatalytic oxidation would be much more important than that of the ATD particles of this study. To extend the AMAR model derived with ATD particle to ambient dust particles, the model parameters related to the rate constants and

physical characteristics (e.g., surface area and hygroscopic properties) of dust particles need to be modified using laboratory studies. Photocatalytic capacities of authentic mineral dust would be different from ATD due to the compositions and quantity of conductive metal oxides. Hence, the photoactivation rate constant ( $k_{e-h}^j$  in Sect. 3.2.3) to form electron-hole pairs should also be revisited to apply the present model to different mineral dust systems. In addition to reactions of inorganic species (i.e.,  $\text{SO}_2$  and  $\text{NO}_x$ ), that of organic species (e.g.,  $\text{HCOOH}$ ,  $\text{HCHO}$ , and  $\text{CH}_3\text{CHO}$ ) on dust surface needs to be investigated in the future.

**Data availability.** The datasets generated during the current study are available from the corresponding author on reasonable request.

**The Supplement related to this article is available online at <https://doi.org/10.5194/acp-17-10001-2017-supplement>.**

**Competing interests.** The authors declare that they have no conflict of interest.

**Acknowledgements.** This work was supported by grants from the National Institute of Metrological Science (NIMS-2016-3100), the Ministry of Science, ICT, and Future Planning at South Korea (2014M3C8A5032316) and the Fulbright Scholar Program (from USA to Mongolia).

Edited by: Barbara Ervens

Reviewed by: two anonymous referees

## References

Adams, J. W., Rodriguez, D., and Cox, R. A.: The uptake of  $\text{SO}_2$  on Saharan dust: a flow tube study, *Atmos. Chem. Phys.*, 5, 2679–2689, <https://doi.org/10.5194/acp-5-2679-2005>, 2005.

Atkinson, R. and Lloyd, A. C.: Evaluation of kinetic and mechanistic data for modeling of photochemical smog, *J. Phys. Chem. Ref. Data*, 13, 315–444, <https://doi.org/10.1063/1.555710>, 1984.

Atkinson, R., Baulch, D., Cox, R., Hampson Jr., R., Kerr, J., Rossi, M., and Troe, J.: Evaluated kinetic and photochemical data for atmospheric chemistry: supplement VI, IUPAC subcommittee on gas kinetic data evaluation for atmospheric chemistry, *J. Phys. Chem. Ref. Data*, 26, 1329–1499, 1997.

Baulch, D., Cox, R., Hampson Jr., R., Kerr, J., Troe, J., and Watson, R.: Evaluated kinetic and photochemical data for atmospheric chemistry: supplement II. CODATA task group on gas 20 phase chemical kinetics, *J. Phys. Chem. Ref. Data*, 13, 1259–1380, <https://doi.org/10.1063/1.555721>, 1984.

Beardsley, R., Jang, M., Ori, B., Im, Y., Delcomyn, C. A., and Witherspoon, N.: Role of sea salt aerosols in the formation of aromatic secondary organic aerosol: yields and hygroscopic properties, *Environ. Chem.*, 10, 167–177, <https://doi.org/10.1071/En13016>, 2013.

Beardsley, R. L. and Jang, M.: Simulating the SOA formation of isoprene from partitioning and aerosol phase reactions in the presence of inorganics, *Atmos. Chem. Phys.*, 16, 5993–6009, <https://doi.org/10.5194/acp-16-5993-2016>, 2016.

Becker, K. H., Kleffmann, J., Kurtenbach, R., and Wiesen, P.: Solubility of nitrous acid (HONO) in sulfuric acid solutions, *J. Phys. Chem.*, 100, 14984–14990, 1996.

Binkowski, F. S. and Roselle, S. J.: Models-3 Community Multiscale Air Quality (CMAQ) model aerosol component 1. Model description, *J. Geophys. Res.-Atmos.*, 108, <https://doi.org/10.1029/2001JD001409>, 2003.

Bond, T. C.: Spectral dependence of visible light absorption by carbonaceous particles emitted from coal combustion, *Geophys. Res. Lett.*, 28, 4075–4078, <https://doi.org/10.1029/2001gl013652>, 2001.

Bongartz, A., Kames, J., Welter, F., and Schurath, U.: Near-UV absorption cross sections and trans/cis equilibrium of nitrous acid, *J. Phys. Chem.*, 95, 1076–1082, 1991.

Byun, D. and Schere, K. L.: Review of the governing equations, computational algorithms, and other components of the models-3 Community Multiscale Air Quality (CMAQ) modeling system, *Appl. Mech. Rev.*, 59, 51–77, <https://doi.org/10.1115/1.2128636>, 2006.

Calvert, J. G. and Stockwell, W.: Mechanism and rates of the gas phase oxidations of sulfur dioxide and the nitrogen oxides in the atmosphere, Ohio State Univ., Columbus (USA), Dept. of Chemistry, 1983.

Chameides, W. L.: The photochemistry of a remote marine stratiform cloud, *J. Geophys. Res.-Atmos.*, 89, 4739–4755, 1984.

Chang, R. Y. W., Sullivan, R. C., and Abbott, J. P. D.: Initial uptake of ozone on Saharan dust at atmospheric relative humidities, *Geophys. Res. Lett.*, 32, L14815, <https://doi.org/10.1029/2005gl023317>, 2005.

Chen, H. H., Nanayakkara, C. E., and Grassian, V. H.: Titanium Dioxide Photocatalysis in Atmospheric Chemistry, *Chem. Rev.*, 112, 5919–5948, <https://doi.org/10.1021/cr3002092>, 2012.

Clegg, S. and Wexler, A. S.: Densities and Apparent Molar Volumes of Atmospherically Important Electrolyte Solutions. 2. The Systems  $\text{H}^+ \cdot \text{HSO}_4^- \cdot \text{SO}_4^{2-} \cdot \text{H}_2\text{O}$  from 0 to 3 mol kg $^{-1}$  as a Function of Temperature and  $\text{H}^+ \cdot \text{NH}_4^+ \cdot \text{HSO}_4^- \cdot \text{SO}_4^{2-} \cdot \text{H}_2\text{O}$  from 0 to 6 mol kg $^{-1}$  at 25°C Using a Pitzer Ion Interaction Model, and  $\text{NH}_4\text{HSO}_4 \cdot \text{H}_2\text{O}$  and  $(\text{NH}_4)_3\text{H}(\text{SO}_4)_2 \cdot \text{H}_2\text{O}$  over the Entire Concentration Range, *J. Phys. Chem. A*, 115, 3461–3474, 2011.

Clegg, S. L., Brimblecombe, P., and Wexler, A. S.: Thermodynamic model of the system  $\text{H}^+ \cdot \text{NH}_4^+ \cdot \text{SO}_4^{2-} \cdot \text{NO}_3^- \cdot \text{H}_2\text{O}$  at tropospheric temperatures, *J. Phys. Chem. A*, 102, 2137–2154, 1998.

Colberg, C. A., Luo, B. P., Wernli, H., Koop, T., and Peter, Th.: A novel model to predict the physical state of atmospheric  $\text{H}_2\text{SO}_4/\text{NH}_3/\text{H}_2\text{O}$  aerosol particles, *Atmos. Chem. Phys.*, 3, 909–924, <https://doi.org/10.5194/acp-3-909-2003>, 2003.

Colmenares, J. C. and Luque, R.: Heterogeneous photocatalytic nanomaterials: prospects and challenges in selective transformations of biomass-derived compounds, *Chem. Soc. Rev.*, 43, 765–778, <https://doi.org/10.1039/c3cs60262a>, 2014.

Crowley, J. N., Ammann, M., Cox, R. A., Hynes, R. G., Jenkin, M. E., Mellouki, A., Rossi, M. J., Troe, J., and Wallington, T. J.: Evaluated kinetic and photochemical data for at-

mospheric chemistry: Volume V – heterogeneous reactions on solid substrates, *Atmos. Chem. Phys.*, 10, 9059–9223, <https://doi.org/10.5194/acp-10-9059-2010>, 2010.

Cwiertny, D. M., Young, M. A., and Grassian, V. H.: Chemistry and photochemistry of mineral dust aerosol, *Annu. Rev. Phys. Chem.*, 59, 27–51, <https://doi.org/10.1146/annurev.physchem.59.032607.093630>, 2008.

Dong, X., Fu, J. S., Huang, K., Tong, D., and Zhuang, G.: Model development of dust emission and heterogeneous chemistry within the Community Multiscale Air Quality modeling system and its application over East Asia, *Atmos. Chem. Phys.*, 16, 8157–8180, <https://doi.org/10.5194/acp-16-8157-2016>, 2016.

Dupart, Y., King, S. M., Nekat, B., Nowak, A., Wiedensohler, A., Herrmann, H., David, G., Thomas, B., Miffre, A., Raioux, P., D'Anna, B., and George, C.: Mineral dust photochemistry induces nucleation events in the presence of  $\text{SO}_2$ , *P. Natl. Acad. Sci. USA*, 109, 20842–20847, <https://doi.org/10.1073/pnas.1212297109>, 2012.

Dupart, Y., Fine, L., D'Anna, B., and George, C.: Heterogeneous uptake of  $\text{NO}_2$  on Arizona Test Dust under UV-A irradiation: An aerosol flow tube study, *Aeolian Res.*, 15, 45–51, <https://doi.org/10.1016/j.aeolia.2013.10.001>, 2014.

Gankanda, A., Coddens, E. M., Zhang, Y., Cwiertny, D. M., and Grassian, V. H.: Sulfate formation catalyzed by coal fly ash, mineral dust and iron (iii) oxide: variable influence of temperature and light, *Environ. Sci.*, 18, 1484–1491, 2016.

Goodman, A. L., Li, P., Usher, C. R., and Grassian, V. H.: Heterogeneous uptake of sulfur dioxide on aluminum and magnesium oxide particles, *J. Phys. Chem. A*, 105, 6109–6120, <https://doi.org/10.1021/jp004423z>, 2001.

Graedel, T.: The homogeneous chemistry of atmospheric sulfur, *Rev. Geophys.*, 15, 421–428, 1977.

Gustafsson, R. J., Orlov, A., Badger, C. L., Griffiths, P. T., Cox, R. A., and Lambert, R. M.: A comprehensive evaluation of water uptake on atmospherically relevant mineral surfaces: DRIFT spectroscopy, thermogravimetric analysis and aerosol growth measurements, *Atmos. Chem. Phys.*, 5, 3415–3421, <https://doi.org/10.5194/acp-5-3415-2005>, 2005.

Hoffmann, M. R., Martin, S. T., Choi, W. Y., and Bahnenmann, D. W.: Environmental Applications of Semiconductor Photocatalysis, *Chem. Rev.*, 95, 69–96, <https://doi.org/10.1021/cr00033a004>, 1995.

Hoyle, C. R., Fuchs, C., Järvinen, E., Saathoff, H., Dias, A., El Haddad, I., Gysel, M., Coburn, S. C., Tröstl, J., Bernhammer, A.-K., Bianchi, F., Breitenlechner, M., Corbin, J. C., Craven, J., Donahue, N. M., Duplissy, J., Ehrhart, S., Frege, C., Gordon, H., Höppel, N., Heinritzi, M., Kristensen, T. B., Molteni, U., Nichman, L., Pinterich, T., Prévôt, A. S. H., Simon, M., Slowik, J. G., Steiner, G., Tomé, A., Vogel, A. L., Volkamer, R., Wagner, A. C., Wagner, R., Wexler, A. S., Williamson, C., Winkler, P. M., Yan, C., Amorim, A., Dommen, J., Curtius, J., Gallagher, M. W., Flanagan, R. C., Hansel, A., Kirkby, J., Kulmala, M., Möhler, O., Stratmann, F., Worsnop, D. R., and Baltensperger, U.: Aqueous phase oxidation of sulphur dioxide by ozone in cloud droplets, *Atmos. Chem. Phys.*, 16, 1693–1712, <https://doi.org/10.5194/acp-16-1693-2016>, 2016.

Huang, L. B., Zhao, Y., Li, H., and Chen, Z. M.: Kinetics of Heterogeneous Reaction of Sulfur Dioxide on Authentic Mineral Dust: Effects of Relative Humidity and Hydrogen Peroxide, *Environ. Sci. Technol.*, 49, 10797–10805, <https://doi.org/10.1021/acs.est.5b03930>, 2015.

Jang, J., Jang, M., Mui, W., Delcomyn, C. A., Henley, M. V., and Hearn, J. D.: Formation of active chlorine oxidants in saline-oxone aerosol, *Aerosol Sci. Tech.*, 44, 1018–1026, 2010.

Jeffries, H. E., Gary, M. W., Kessler, M., and Sexton, K. G.: Morpheme reaction mechanism, MORPHO, ALLOMORPHIC simulation software, 1998.

Kerr, J. and Calvert, J.: Chemical Transformation Modules for Eulerian Acid Decomposition Models, Volume I: The gas-phase chemistry, Boulder, Colorado, 1984.

Krueger, B. J., Grassian, V. H., Laskin, A., and Cowin, J. P.: The transformation of solid atmospheric particles into liquid droplets through heterogeneous chemistry: Laboratory insights into the processing of calcium containing mineral dust aerosol in the troposphere, *Geophys. Res. Lett.*, 30, 1148, <https://doi.org/10.1029/2002gl016563>, 2003.

Li, J. and Jang, M.: Aerosol acidity measurement using colorimetry coupled with a reflectance UV-visible spectrometer, *Aerosol. Sci. Tech.*, 46, 833–842, 2012.

Li, J., Jang, M., and Beardsley, R. L.: Dialkylsulfate formation in sulfuric acid-seeded secondary organic aerosol produced using an outdoor chamber under natural sunlight, *Environ. Chem.*, 13, 590–601, <https://doi.org/10.1071/EN15129>, 2015.

Li, J. W. and Han, Z. W.: A modeling study of the impact of heterogeneous reactions on mineral aerosol surfaces on tropospheric chemistry over East Asia, *Particuology*, 8, 433–441, <https://doi.org/10.1016/j.partic.2010.03.018>, 2010.

Liang, J. Y. and Jacobson, M. Z.: A study of sulfur dioxide oxidation pathways over a range of liquid water contents, pH values, and temperatures, *J Geophys Res-Atmos.*, 104, 13749–13769, <https://doi.org/10.1029/1999jd900097>, 1999.

Linsebigler, A. L., Lu, G. Q., and Yates, J. T.: Photocatalysis on  $\text{TiO}_2$  Surfaces – Principles, Mechanisms, and Selected Results, *Chem. Rev.*, 95, 735–758, <https://doi.org/10.1021/cr00035a013>, 1995.

Liu, C., Ma, Q. X., Liu, Y. C., Ma, J. Z., and He, H.: Synergistic reaction between  $\text{SO}_2$  and  $\text{NO}_2$  on mineral oxides: a potential formation pathway of sulfate aerosol, *Phys. Chem. Chem. Phys.*, 14, 1668–1676, <https://doi.org/10.1039/c1cp22217a>, 2012.

Liu, Y. J., Zhu, T., Zhao, D. F., and Zhang, Z. F.: Investigation of the hygroscopic properties of  $\text{Ca}(\text{NO}_3)_2$  and internally mixed  $\text{Ca}(\text{NO}_3)_2/\text{CaCO}_3$  particles by micro-Raman spectrometry, *Atmos. Chem. Phys.*, 8, 7205–7215, <https://doi.org/10.5194/acp-8-7205-2008>, 2008.

Ma, Q. X., Liu, Y. C., and He, H.: Synergistic effect between  $\text{NO}_2$  and  $\text{SO}_2$  in their adsorption and reaction on gamma-alumina, *J. Phys. Chem. A.*, 112, 6630–6635, <https://doi.org/10.1021/jp802025z>, 2008.

Martell, A. E. and Smith, R. M.: Inorganic complexes, Plenum Press, 1976.

McNaught, A. D. and Wilkinson, A.: IUPAC, Compendium of Chemical Terminology, the “Gold Book”, Wiley Blackwell, 2nd revised Edn., 1997.

Michel, A. E., Usher, C. R., and Grassian, V. H.: Reactive uptake of ozone on mineral oxides and mineral dusts, *Atmos. Environ.*, 37, 3201–3211, [https://doi.org/10.1016/S1352-2310\(03\)00319-4](https://doi.org/10.1016/S1352-2310(03)00319-4), 2003.

Nanayakkara, C. E., Pettibone, J., and Grassian, V. H.: Sulfur dioxide adsorption and photooxidation on isotopically-labeled titanium dioxide nanoparticle surfaces: roles of surface hydroxyl groups and adsorbed water in the formation and stability of adsorbed sulfite and sulfate, *Phys. Chem. Chem. Phys.*, 14, 6957–6966, <https://doi.org/10.1039/c2cp23684b>, 2012.

Navea, J. G., Chen, H. H., Huang, M., Carmichael, G. R., and Grassian, V. H.: A comparative evaluation of water uptake on several mineral dust sources, *Environ. Chem.*, 7, 162–170, <https://doi.org/10.1071/En09122>, 2010.

Park, J. and Jang, M.: Heterogeneous photooxidation of sulfur dioxide in the presence of airborne mineral dust particles, *RSC Advances*, 6, 58617–58627, 2016.

Reyes-Coronado, D., Rodríguez-Gattorno, G., Espinosa-Pesqueira, M., Cab, C., De Coss, R., and Oskam, G.: Phase-pure  $\text{TiO}_2$  nanoparticles: anatase, brookite and rutile, *Nanotechnology*, 19, 145605, <https://doi.org/10.1088/0957-4484/19/14/145605>, 2008.

Saliba, N. A. and Chamseddine, A.: Uptake of acid pollutants by mineral dust and their effect on aerosol solubility, *Atmos. Environ.*, 46, 256–263, <https://doi.org/10.1016/j.atmosenv.2011.09.074>, 2012.

Saliba, N. A., Moussa, S. G., and El Tayyar, G.: Contribution of airborne dust particles to HONO sources, *Atmos. Chem. Phys. Discuss.*, 14, 4827–4839, <https://doi.org/10.5194/acpd-14-4827-2014>, 2014.

Sarwar, G., Fahey, K., Kwok, R., Gilliam, R. C., Roselle, S. J., Mathur, R., Xue, J., Yu, J., and Carter, W. P.: Potential impacts of two  $\text{SO}_2$  oxidation pathways on regional sulfate concentrations: aqueous-phase oxidation by  $\text{NO}_2$  and gas-phase oxidation by Stabilized Criegee Intermediates, *Atmos. Environ.*, 68, 186–197, 2013.

Sarwar, G., Simon, H., Fahey, K., Mathur, R., Goliff, W. S., and Stockwell, W. R.: Impact of sulfur dioxide oxidation by Stabilized Criegee Intermediate on sulfate, *Atmos. Environ.*, 85, 204–214, 2014.

Schwartz, S. and White, W.: Solubility equilibria of the nitrogen oxides and oxyacids in dilute aqueous solution, *Adv. Environ. Sci. Eng.*, United States, 4, 1–45, 1981.

Schwartz, S. E.: Gas-Phase and Aqueous-Phase Chemistry of  $\text{HO}_2$  in Liquid Water Clouds, *J. Geophys. Res.-Atmos.*, 89, 1589–1598, <https://doi.org/10.1029/JD089iD07p11589>, 1984.

Shang, J., Li, J., and Zhu, T.: Heterogeneous reaction of  $\text{SO}_2$  on  $\text{TiO}_2$  particles, *Sci. China Chem.*, 53, 2637–2643, [doi:10.1007/s11426-010-4160-3](https://doi.org/10.1007/s11426-010-4160-3), 2010.

Tang, M. J., Cziczo, D. J., and Grassian, V. H.: Interactions of Water with Mineral Dust Aerosol: Water Adsorption, Hygroscopicity, Cloud Condensation, and Ice Nucleation, *Chem. Rev.*, 116, 4205–4259, <https://doi.org/10.1021/acs.chemrev.5b00529>, 2016.

Tang, Y. H., Carmichael, G. R., Kurata, G., Uno, I., Weber, R. J., Song, C. H., Guttikunda, S. K., Woo, J. H., Streets, D. G., Wei, C., Clarke, A. D., Huebert, B., and Anderson, T. L.: Impacts of dust on regional tropospheric chemistry during the ACE-Asia experiment: A model study with observations, *J. Geophys. Res.-Atmos.*, 109, D19s21, <https://doi.org/10.1029/2003jd003806>, 2004.

Thiebaud, J., Thevenet, F., and Fittschen, C.: OH Radicals and  $\text{H}_2\text{O}_2$  Molecules in the Gas Phase near to  $\text{TiO}_2$  Surfaces, *J. Phys. Chem. C*, 114, 3082–3088, <https://doi.org/10.1021/jp9102542>, 2010.

Thompson, T. L. and Yates, J. T.: Surface science studies of the photoactivation of  $\text{TiO}_2$  new photochemical processes, *Chem. Rev.*, 106, 4428–4453, 2006.

Ullerstam, M., Vogt, R., Langer, S., and Ljungstrom, E.: The kinetics and mechanism of  $\text{SO}_2$  oxidation by  $\text{O}_3$  on mineral dust, *Phys. Chem. Chem. Phys.*, 4, 4694–4699, <https://doi.org/10.1039/b203529b>, 2002.

Underwood, G. M., Song, C. H., Phadnis, M., Carmichael, G. R., and Grassian, V. H.: Heterogeneous reactions of  $\text{NO}_2$  and  $\text{HNO}_3$  on oxides and mineral dust: A combined laboratory and modeling study, *J. Geophys. Res.-Atmos.*, 106, 18055–18066, <https://doi.org/10.1029/2000jd900552>, 2001.

Usher, C. R., Al-Hosney, H., Carlos-Cuellar, S., and Grassian, V. H.: A laboratory study of the heterogeneous uptake and oxidation of sulfur dioxide on mineral dust particles, *J. Geophys. Res.-Atmos.*, 107, 4713, <https://doi.org/10.1029/2002jd002051>, 2002.

Usher, C. R., Michel, A. E., Stec, D., and Grassian, V. H.: Laboratory studies of ozone uptake on processed mineral dust, *Atmos. Environ.*, 37, 5337–5347, <https://doi.org/10.1016/j.atmosenv.2003.09.014>, 2003.

Vlasenko, A., Sjogren, S., Weingartner, E., Stemmler, K., Gäggeler, H. W., and Ammann, M.: Effect of humidity on nitric acid uptake to mineral dust aerosol particles, *Atmos. Chem. Phys.*, 6, 2147–2160, <https://doi.org/10.5194/acp-6-2147-2006>, 2006.

Wagner, C., Schuster, G., and Crowley, J.: An aerosol flow tube study of the interaction of  $\text{N}_2\text{O}_5$  with calcite, Arizona dust and quartz, *Atmos. Environ.*, 43, 5001–5008, 2009.

Wagner, R., Ajtai, T., Kandler, K., Lieke, K., Linke, C., Müller, T., Schnaiter, M., and Vragel, M.: Complex refractive indices of Saharan dust samples at visible and near UV wavelengths: a laboratory study, *Atmos. Chem. Phys.*, 12, 2491–2512, <https://doi.org/10.5194/acp-12-2491-2012>, 2012.

Wexler, A. S. and Clegg, S. L.: Atmospheric aerosol models for systems including the ions  $\text{H}^+$ ,  $\text{NH}_4^+$ ,  $\text{Na}^+$ ,  $\text{SO}_4^{2-}$ ,  $\text{NO}_3^-$ ,  $\text{Cl}^-$ ,  $\text{Br}^-$ , and  $\text{H}_2\text{O}$ , *J. Geophys. Res.-Atmos.*, 107, <https://doi.org/10.1029/2001JD000451>, 2002.

Zhang, X. Y., Zhuang, G. S., Chen, J. M., Wang, Y., Wang, X., An, Z. S., and Zhang, P.: Heterogeneous reactions of sulfur dioxide on typical mineral particles, *J. Phys. Chem. B*, 110, 12588–12596, <https://doi.org/10.1021/jp0617773>, 2006.

Zhang, Y.-H. and Chan, C. K.: Understanding the hygroscopic properties of supersaturated droplets of metal and ammonium sulfate solutions using Raman spectroscopy, *J. Phys. Chem. A*, 106, 285–292, 2002.

Zhong, M. and Jang, M.: Light absorption coefficient measurement of SOA using a UV-Visible spectrometer connected with an integrating sphere, *Atmos. Environ.*, 45, 4263–4271, <https://doi.org/10.1016/j.atmosenv.2011.04.082>, 2011.

Zuend, A., Marcolli, C., Booth, A. M., Lienhard, D. M., Soon-sin, V., Krieger, U. K., Topping, D. O., McFiggans, G., Peter, T., and Seinfeld, J. H.: New and extended parameterization of the thermodynamic model AIOMFAC: calculation of activity coefficients for organic-inorganic mixtures containing carboxyl, hydroxyl, carbonyl, ether, ester, alkenyl, alkyl, and aromatic functional groups, *Atmos. Chem. Phys.*, 11, 9155–9206, <https://doi.org/10.5194/acp-11-9155-2011>, 2011.